Atmos. Chem. Phys. Discuss., 13, 4331–4389, 2013
www.atmos-chem-phys-discuss.net/13/4331/2013/
doi:10.5194/acpd-13-4331-2013

Atmospheric Chemistry and Physics Discussions

On the relationship between Arctic ice clouds and polluted air masses over the north slope of Alaska in April 2008

C. Jouan[1,2], J. Pelon[2], E. Girard[1], G. Ancellet[2], J. P. Blanchet[1], and J. Delanoë[3]

[1]ESCER Centre, Department of Earth and Atmospheric Sciences, University of Quebec at Montreal, H3C 3P8, Montreal, Quebec, Canada
[2]Laboratoire Atmosphère, Milieux et Observations Spatiales, UMR8190, UPMC, 75252, Paris, France
[3]Laboratoire Atmosphère, Milieux et Observations Spatiales, UVSQ, 78035, Guyancourt, France

Received: 2 January 2013 – Accepted: 26 January 2013 – Published: 15 February 2013

Correspondence to: C. Jouan (jouan.caroline6@gmail.com) and
J. Pelon (jacques.pelon@latmos.ipsl.fr)

Published by Copernicus Publications on behalf of the European Geosciences Union.

Abstract

Recently, two Types of Ice Clouds (TICs) properties have been characterized using ISDAC airborne measurements (Alaska, April 2008). TIC-2B were characterized by fewer ($< 10\,L^{-1}$) and larger ($> 110\,\mu m$) ice crystals, a larger ice supersaturation ($> 15\,\%$) and a fewer ice nuclei (IN) concentration (< 2 order of magnitude) when compared to TIC-1/2A. It has been hypothesized that emissions of SO_2 may reduce the ice nucleating properties of IN through acidification, resulting to a smaller concentration of larger ice crystals and leading to precipitation (e.g. cloud regime TIC-2B) because of the reduced competition for the same available moisture.

Here, the origin of air masses forming the ISDAC TIC-1/2A (1 April 2008) and TIC-2B (15 April 2008) is investigated using trajectory tools and satellite data. Results show that the synoptic conditions favor air masses transport from the three potentials SO_2 emission areas to Alaska: eastern China and Siberia where anthropogenic and biomass burning emission respectively are produced and the volcanic region from the Kamchatka/Aleutians. Weather conditions allow the accumulation of pollutants from eastern China/Siberia over Alaska, most probably with the contribution of acid volcanic aerosol during the TIC-2B period. OMI observations reveal that SO_2 concentrations in air masses forming the TIC-2B were larger than in air masses forming the TIC-1/2A. Airborne measurements show high acidity near the TIC-2B flight where humidity was low. These results strongly support the hypothesis that acidic coating on IN are at the origin of the formation of TIC-2B.

1 Introduction

Climate change is proceeding faster and more severely at the high latitudes of the Arctic (ACIA, 2005; IPCC, 2007). Average annual Arctic temperature has been increasing at about twice the global mean rate in the past 50 yr. The uncertainties of the amplitude and the evolution of Arctic warming are partly related to a lack of understanding of

ACPD
13, 4331–4389, 2013

the contributions of clouds in the energy balance over this region (Dufresne and Bony, 2008). Clouds play a fundamental role both in modulating atmospheric radiation and the hydrologic cycles. This is particularly critical in the Arctic, where interactions can be enhanced by the presence of aerosols (Grenier and Blanchet, 2010; Morrison et al., 2005).

Arctic cloud properties have been investigated in a number of observational studies using aircraft, ground-based remote sensors and satellites. It was recently shown that ice-only clouds are ubiquitous in the upper troposphere during all seasons in the Arctic (Shupe, 2011; Devasthales et al., 2011). Although optically thin ice clouds may have a small effect on the radiation budget at the surface (Intrieri and Shupe, 2004; Lampert et al., 2009), their existence could be important in the Arctic spring to (1) maintain mixed phase low clouds (Morrison et al., 2005, 2012), or (2) in the winter when the warming resulting from the "cloud greenhouse effect (thermal)" dominates (Girard and Blanchet, 2001; Shupe and Inrieri, 2004). Cloud radiative forcing at the surface strongly depends on cloud properties, solar zenith angle, and surface albedo (Shupe and Intrieri, 2004).

The joint detection characteristics of both CloudSat radar and CALIPSO lidar recently reveal the existence of two Types of Ice Clouds (TICs) (namely TIC-2B and TIC-1/2A) in the Arctic during the polar night and early spring (Grenier et al., 2009; Grenier and Blanchet, 2010). Jouan et al. (2012) have characterized the TICs properties using airborne measurements taken during the ISDAC (Indirect and Semi-Direct Aerosol Campaign) campaign, which was conducted over the North Slope of Alaska (NSA) during April 2008 (McFarquhar et al., 2011). Jouan et al. (2012) also tested the ability of a variational synergistic algorithm (Varcloud), combining both radar and lidar satellite observations and developed by Delanoë and Hogan (2008), to retrieve the ice water content (IWC), extinction and ice crystal effective radius (R_e) in regions of the TICs detected by both of these instruments. Values of the effective radius recovered as a function of the normalized altitude showed that the averaged R_e of the TIC-2B was greater by a factor of $\sim$ 1.3 on the first 2 km at the top of the ice cloud when compared to the averaged R_e of the TIC-1/2A.

ACPD
13, 4331–4389, 2013

From this study, seven ice clouds with low ice water content (IWC) below 0.03 g m^{-3} and air temperature (T_a) colder than −30 °C have been selected. Two types of ice clouds in this sample have been distinguished. TIC-2B clouds are characterized by fewer (< 10 L^{-1}) and larger (> 110 µm) ice crystals and a larger ice supersaturation (by about 15 % to 20 %) when compared to TIC-1/2A. Based on in-situ ice nuclei (IN) concentration measurements available for several flights, it was shown that the IN concentration was two orders of magnitude lower in the TIC-2B ice clouds when compared to the TIC-1/2A ice clouds. Moreover, most of the differences between these two TICs are located near the cloud top where the nucleation of ice crystals is most likely to occur. In TIC-1/2A case, it was suggested that the dominant nucleation process was the deposition ice nucleation due to an atmosphere not saturated with respect to liquid water. In the TIC-2B case, either immersion or condensation freezing of haze droplets (coated IN) was hypothetized, due to larger relative humidity with respect to ice close to liquid water saturation. Low concentrations of IN combined to the high supersaturated air with respect to ice, lead to an explosive growth of ice crystals by water vapor diffusion. As a result, the TIC-2B ice cloud is composed essentially of a relatively low concentration of precipitating ice crystals whereas the TIC-1/2A ice cloud is composed of a top layer of small ice crystals in relatively large concentrations, which slowly grows to precipitating sizes by water vapor diffusion and followed by collision processes.

Northern Pacific Ocean and Alaska are regions were mineral particles potentially acting as IN in the atmosphere since they are frequently transported from China desertic areas (Uno et al., 2009) and volcanic regions such as Aleutian Islands (Alaska, USA) or Kamchatka Peninsula (Russia) (Yalcin et al., 2002). Depending on the process involved (contact or immersion), a high heterogeneous freezing probability for near source samples was found to occur at various temperatures above −25 °C from lab measurements (Durant et al., 2008). However in IN-rich airmasses such as those encountered after a strong desert dust uplift or volcanic eruption, overseeding may lead to a larger number of crystals with smaller crystal sizes depending on available water, which will also depend on the source of particles, as airmasses may keep track

ACPD
13, 4331–4389, 2013

of their origin over days at high altitude. Knowledge of the chemical composition of the ambient ice-forming aerosol particles is important in order to understand the physical process of TICs formation. The major source of wintertime and springtime aerosol in the Arctic comes from long-range transport of mid-latitudes anthropogenic pollution. A winter-spring maximum is known as Arctic haze (Uttal et al., 2002; Law and Stohl, 2007; Hirdman et al., 2010). Sulphate (compounds including the SO_4^{-2} ion) is the dominant component of these pollutant-enriched aerosols (Barrie and Barrie, 1990; Quinn et al., 2007). Volcanic emissions (releasing sulphate precursor sulfur dioxyde (SO_2)), oxidation of biogenic dimethyl sulfide (DMS) and open biomass burning are also important natural sources of sulphate pollution (Fisher et al., 2011; Warneke et al., 2009). SO_2 must be oxidized to form sulphate before playing a role in aerosol nucleation and the modification of existing particles. The chemical transformation of SO_2 to sulphate in the atmosphere can occur via the gas-phase oxidation (cloud-free air) with the hydroxyl radical (OH) and/or via the oxidation in the aqueous-phase (cloud droplets or pre-existing aerosols) with hydrogen peroxide (H_2O_2), ozone (O_3), and iron catalysis as terminating reactions. These reactions are considered to be the most important sulfur dioxide oxidation pathways on a global scale (Seinfeld and Pandis, 1998). The rates of SO_2 oxidation processes are influenced by many factors such as photochemistry, temperature, atmospheric conditions (especially high relative humidity) and concentration and composition of particulate matter (Seinfeld and Pandis, 1998). It will determine the SO_2 lifetime in the atmosphere. Once the SO_2 gets into the cold, dry, arctic air, the residence time of SO_2 should be increased. When SO_2 is released into the atmosphere, around 46–82 % of the SO_2 emitted undergoes chemical transformations and forms sulphate while the rest is lost through dry and wet deposition (IPCC, 2001; Chin et al., 2000). According to Seinfeld and Pandis (1998), SO_2 is chemically active and has a relatively short averaged atmospheric lifetime of $\sim$ 2 days while sulphate-containing aerosols have an averaged lifetime of $\sim$ 4–5 days (Adams et al., 1999). The sulphate in aerosol particles is present as sulfuric acid (H_2SO_4), ammonium sulphate ($(NH_4)_2SO_4$),

ACPD
13, 4331–4389, 2013

or intermediate compounds, depending on the availability of gaseous ammonia (NH_3) to neutralize the sulfuric acid (Khoder, 2002).

The hydrophilic property of most sulphate compounds, especially sulfuric acid, makes them particularly efficient as condensation nuclei (CN). Sulphate particles are thus often found as solution droplets in the atmosphere (when not frozen). The role of sulphate in ice nucleation is not well known. Recent laboratory experiments have shown that good ice nuclei such as mineral dust are "de-activated" when they are coated with various species such as ammonium sulphate, ammonium bi-sulphate, sulfuric acid and some organics (e.g. Eastwood et al., 2009; Chernoff et al., 2010). These experiments have shown that the onset ice supersaturation at which ice nucleation occurs (in the immersion mode of unactivated haze droplets) is substantially increased close to the liquid saturation point when the kaolinite particles are coated with sulfuric acid compared to uncoated particles (in the deposition mode). According to Sullivan et al. (2010), the IN de-activation effect of sulphuric acid on dust particle is irreversible and still effective once the acid has been neutralized with ammonia.

Blanchet and Girard (1994) and Grenier et al. (2009, 2010) have hypothesized that the decrease of the ice nuclei concentration associated to highly acidic aerosols leads to a smaller concentration of ice crystals. Because of the reduced competition for the same available moisture, ice crystals reach larger sizes. As a result, large ice crystals form in relatively small concentrations, leading to precipitation, e.g. cloud regime TIC-2B. Therefore, the ice crystal precipitation rate and the rate of dehydration of the lower troposphere increase while the water vapor and TIC-2B greenhouse effect decrease at the expense of non-precipitating ice clouds. At cold Arctic winter temperature, the greenhouse effect in the so-called dirty window (17 to 35 µm) is especially sensitive to atmospheric dehydration. Positive feedback is created between the mid- and lower-troposphere cooling and dehydration efficiency, increasing the production rate of cold and dry air masses. This process is referred to as the Dehydration Greenhouse Feedback (DGF) (Blanchet and Girard, 1994; Girard, 1998). During winter, the extent

ACPD
13, 4331–4389, 2013

to which sulphate coated-aerosol is neutralized can have an important effect on cloud microphysics and on the surface energy budget of the Arctic.

In this paper, the origin of the air masses in which the ISDAC TIC-1/2A (1 April 2008) and TIC-2B form (15 April 2008), identified in Jouan et al. (2012), is investigated to verify the hypothesis regarding the potential link between acidic aerosols and TIC-2B, considering information gathered from the ARCTAS-A (Arctic Research of the Composition of the Troposphere from Aircraft and Satellites – April 2008 – Alaska) (Jacob et al., 2010) and ISDAC field experiments and trajectory analyses. This paper is organized as follows. In Sect. 2, temporal variability of Alaska-averaged sulfur dioxide pollution from satellite data is presented with the meteorological conditions associated during March-April 2008. Sections 3 and 4 list the main potential sources of sulfur dioxide and transport pathway in Alaska during this reporting period, using a lagrangian approach with the FLEXPART model for the study of the long-range transport. Detailed analysis of sources and characteristics of air masses measured on TIC-1/2A and TIC-2B specific cases, investigated in details in Jouan et al. (2012) during the ISDAC campaign, are carried out in the Sect. 5. Results are discussed by examining the CALIPSO satellite tracks, which intersects the back trajectories in the region away from the airborne measurements. A discussion and conclusions are presented in Sects. 6 and 7, respectively.

2 Alaskan pollution and meteorological conditions in April 2008

Satellite measurements provide complementary information on the atmospheric abundance of various gas species. In this study, the ability of the UV (Ultraviolet) and visible spectrometer OMI (Ozone Monitoring Instrument) was used to detect sulfur dioxide. OMI is flying on board the NASA's Earth Observing System (EOS) Aura satellite since July 2004. Aura is a polar orbiting satellite with a nadir ground foot print of $13 \times 24\,km^2$ and a 2600 km cross track swath providing daily and contiguous global mapping of the trace gas species.

ACPD
13, 4331–4389, 2013

The operational OMI SO_2 algorithms require an a priori assumption of SO_2 vertical distribution. For each OMI footprint, OMI SO_2 data products provide four values of total SO_2 column density: SO_2 in the Planetary Boundary Layer (PBL, below 2 km) from anthropogenic sources SO_2 in the lower troposphere (TRL, between 0 to 5 km), mid-troposphere (TRM, between 5 to 10 km) and upper troposphere or lower stratosphere (STL, between 15 to 20 km); all optimized for volcanic activities. These algorithms use the SO_2 absorption bands between 310 and 360 nm to retrieve the column density of SO_2. PBL SO_2 data are derived using the Band Residual Difference (BRD) algorithm (Krotkov et al., 2006). SO_2 data for the other altitudes (TRL, TRM, STL) are retrieved using the Linear Fit (LF) algorithm (Yang et al., 2007). The user must select the most appropriate SO_2 product for the prevailing geophysical conditions. The SO_2 from industrial air pollution is likely to be confined to the PBL, while SO_2 from effusive eruptions or degassing of volcanoes is likely to spread in the free troposphere from the summit of the volcano to 5–10 km altitude (Yang et al., 2007). The total SO_2 column density is given in Dobson Units ($1\,\mathrm{DU} = 2.69 \times 10^{16}\,\mathrm{molecules\,cm^{-2}}$).

The OMI Level 2G daily gridded ($0.125 \times 0.125^{\circ}$) SO_2 products are used to assess qualitatively the temporal variability of SO_2 over the study area of Alaska. OMI L2G SO_2 products were acquired using the GES-DISC Interactive Online Visualization ANd aNalysis Infrastructure (GIOVANNI) developed by the NASA Goddard Earth Sciences (GES) Data and Information Services Center (DISC). OMI L2G SO_2 products were filtered to remove data with high radiative cloud fraction (> 0.3), large solar zenith angle ($> 70^{\circ}$) and anomalous scenes. Data include only those for which the Quality Flags bit 0 was not set, and thus defined as "good data" (GIOVANNI website: http://disc.sci.gsfc.nasa.gov/giovanni/overview/index.html). For example, the standard deviation of TRM retrievals in background areas is about 0.3 DU at mid-latitudes. Both the bias and standard deviation increase with solar zenith angle.

Recent validation of OMI total SO_2 column density measurements confirms that OMI is an effective tool for evaluation of anthropogenic and natural SO_2 emissions. Good qualitative agreement was found between airborne and OMI measurements for the

ACPD
13, 4331–4389, 2013

low altitude anthropogenic sources (Krotkov et al., 2008) as well as strong quantitative agreement between ground-based, airborne and OMI measurements for both eruptive and non-eruptive volcanic emissions at higher altitudes (Spinei et al., 2010; Lopez et al., 2013). However, in each case, the analyses were performed just above the area of emission of SO_2 putting aside the question of the ability of OMI to discriminate sources of SO_2. Preliminary surveys of volcanic OMI SO_2 data indicate that the OMI's detection limit for high latitude and springtime conditions varies from ~ 2000 to 4000 tons of sulfur dioxide emitted per day (Lopez et al., 2013). Detection of weaker sources usually requires temporal averaging of the OMI SO_2 data.

The daily variability of the area-averaged SO_2 total column above Alaska (studied area can be seen in Fig. 1) in mid-troposphere from 27 March to 25 April 2008, shown in Fig. 2, is characterized by periods of lower and higher SO_2 levels. As already mentioned above, most of the differences between TICs are located near the cloud top where the nucleation of ice crystals is most likely to occur, which is why the SO_2 concentrations observed by OMI in the mid-troposphere will be used. Two mean periods were distinguished. The period A (27 March–9 April) is characterized by a relatively low concentration of SO_2 in the range of 0 to 0.12 DU. The period B (10–25 April) is characterized by a concentration of SO_2 3 times higher when compared to the Period A, in the range of 0.06 to 0.39 DU. Peaks of high concentrations are recorded between 13 to 15 April and 20 April, with values greater than 0.25 DU. These SO_2 column amount were calculated based on an assumed SO_2 altitude ranging from 5 to 10 km (TRM OMI L2G SO_2 products) and averaged over the region of Alaska. They should be considered preliminary estimates. Atkinson et al. (2011) analyzed the temporal evolution of sulfur species over the period 25 March through 30 April 2008 from a DRUM impact sampler system operating at 50 km north of Fairbanks. In agreement with the OMI results, the authors notice a low concentration of sulfur ($< 50\,ng\,m^{-3}$) during the first week of April followed by a period of high concentration of sulfur 2–4 times higher than the first week from 7 to 29 April 2008. The observed variations may originate from changes in source intensity and/or from interactions and modification processes during

ACPD
13, 4331–4389, 2013

transport. Only SO_2 observations from OMI in the upper part of the troposphere are considered in this paper. When lifted to the free troposphere (higher than 2000 m), the atmospheric SO_2 has a longer lifetime, and the long-range transport of atmospheric SO_2 from China, for exemple, becomes more efficient (Tu et al., 2004). It is however expected that part of tropospheric SO_2 is removed by dry deposition or oxidization to form sulphate aerosols during transport to Alaska. He et al. (2012) investigated the budget and transport of SO_2 and sulphate in central and eastern China in April 2008 using the Community Multiscale Air Quality (CMAQ) model to simulate sulfur chemistry. Numerical simulations indicate that ~ 50 % of the anthropogenic sulfur emissions were transported downwind, and the overall lifetime of tropospheric SO_2 was 38 ± 7 h, which may cause a more difficult detection of SO_2 after 2–3 days. Then it should be consider that cloud processing and wet deposition may also be a source of modification during transport which may differ during both periods.

Moreover, several factors can change the OMI SO_2 signal: chemical reaction of SO_2 can reduce the signal as lofting of the plume (change of SO_2 vertical distribution) can enhance the signal.

During period A.1 (27 March–2 April), the synoptic pattern was dominated by the presence of a main low-pressure system over the Siberian coast (above the Laptevykh Sea) with a series of low-pressure systems forming over Japan and moving slowly north northeastward toward the Bering Sea (see Fig. 3a). This synoptic pattern sets up a flow trajectory directed initially to the eastern China/Siberia to the east northeastward toward the Aleutians into Alaska. During period A.2 (3–9 April), the main low-pressure system moved up into Alaska; the latter, combined with the anticyclone in the central North Pacific, pushes the Asian exit flow eastward without passing through Alaska from 3–9 April 2008 (see Fig. 3b).

Period B (10–25 April) was dominated by two distinct synoptic patterns. From 10 to 16 April (period B.1), the weakening of the low-pressure system over Alaska and the persistence of the high-pressure system in the central North Pacific allow the establishment of a more zonal pattern in the north that pushes the Asian exit flow northwards

ACPD
13, 4331–4389, 2013

into Alaska and the Siberian exit flow directly eastward into Alaska (see Fig. 3c). Between the 17 and 25 April (period B.2), the anticyclone in the central North Pacific was split into two weaker high-pressure systems by the incursion of a low-pressure system between them. Further north, the combination of a low-pressure system from the west into the Kamchatka/Aleutians with a high-pressure system into the Alaska took place (see Fig. 3d). This leads to the formation of a pressure ridge, thus increasing the transport distance between northeastern China/southeastern Siberia and Alaska. These results suggest that the synoptic conditions encountered during periods A.1, B.1 and B.2 favor air mass transport from eastern Asia/Siberia to Alaska via the volcanic area, with a longer travel time during period B.2. However, the synoptic pattern on Period A promotes air mass transport over a long distance above the North Pacific Ocean providing opportunity to aerosol loss by wet deposition into the marine convective boundary layer, whereas the time of air masses spent over the ocean is significantly shorter during the period B. This could explain the high concentration of SO_2 accumulated during B above Alaska compared to the period A.

3 Potential sources of SO_2 pollution in Alaska

The average column density of SO_2 over April 2008 from anthropogenic sources over the Northern Hemisphere is shown in Fig. 4. In this study, the OMI Level 3 daily gridded ($0.25 \times 0.25^{\circ}$) products (available at http://disc.sci.gsfc.nasa.gov/Aura/data-holdings/OMI/omso2e_v003.shtml) are used to study qualitatively the anthropogenic sources. OMI L3 SO_2 products correspond to the Level 2 PBL SO_2 products filtered for clouds and post-corrected using the methodology of Lee et al. (2009). The standard deviation for this product is ~ 1.5 DU for instantaneous field of view of PBL SO_2 data, but temporal and spatial averaging can reduce the noise by one third. Given this large noise, only SO_2 pollution from strong anthropogenic sources and from strong regional pollution can be detected in daily data (Carn et al., 2007; Krotkov et al., 2008). The highest values, of more than 1.2 DU, are found over eastern China due to the abundance of

ACPD
13, 4331–4389, 2013

coal power plants, metal ores, smelting industry and fossil fuel consumptions in these regions. In April 2008, China was one of the largest contributing countries of sulfur dioxide in the Northern Hemisphere. Lu et al. (2010) estimated the annual SO_2 emission of China to be around ~ 32.1 Tg in 2008.

During the same period, intense Biomass Burning (BB) occurred in southern Russia/Kazakhstan and southeastern Siberia, mainly related to agricultural and boreal forest fires respectively (Warneke et al., 2009, 2010). Figure 5 shows fire activity during April 2008 as indicated by the MODerate resolution Imaging Spectroradiometer (MODIS) fire counts (http://neespi.gsfc.nasa.gov/myd14cm1.shtml) in the Northern Hemisphere. This product presents the total number of fire pixels observed in each grid cell, corrected for multiple satellite overpasses, missing observations, and variable cloud cover.

East Asian anthropogenic emissions and Russian fire emissions contributed to aerosol loading found over the North American Arctic (NAA) during the winter-spring season 2008 (Brock et al., 2011; Jacob et al., 2010; Harrigan et al., 2011). This mixture of anthropogenic sulphate along with BB has followed similar pathways of transport and uplift over the NAA free troposphere (Harrigan et al., 2011) (see Fig. 3). Sulphate aerosols emitted over this area would still be moderately to highly acidic depending on the availability of the large NH_3 source from BB (Fisher et al., 2011).

Volcanoes are another significant natural source and provide emissions of sulphate throughout the troposphere that is not neutralized by natural ammonia emission, thus keeping a higher degree of acidity. There were some volcanic activities over the Aleutian Islands and Kamchatka Peninsula in winter–spring 2008. Continuous degassing activities were common on Cleveland and Veniaminof volcanoes located in the Aleutians. In addition, sustained eruptive activities were recorded at Karymsky and Shiveluch volcanoes located in the Kamchatka Peninsula (see Fig. 1). The Veniaminof and Cleveland volcanoes were monitored by the volcanologists of the Alaska Volcano Observatory (AVO). The Karymsky and Shiveluch volcanoes were monitored by the volcanologists of the Kamchatka Volcanic Eruption Response Team (KVERT). Using seismic

ACPD
13, 4331–4389, 2013

data, satellite images and internet camera data, the daily volcano activity notifications on the websites of AVO (http://www.avo.alaska.edu) and KVERT (http://www.kscnet.ru) noted the presence of persistent activity in Aleutians volcanoes and reported several weak ash-and-gas explosions occurring daily during the reported period in Kamchatka volcanoes. It should be noted that monitoring volcanic eruptions is often challenging due to the remoteness of many of the volcanoes in the region, making a local monitoring network difficult to establish and maintain. Cloudy weather also regularly hinders the ability of satellites to measure SO_2 content and thus detect related eruptions. For these reasons, it is very difficult to quantify the emission of SO_2 above the volcanoes for a long period such as one month.

4 Transport pathways

Three regions of potential SO_2 emissions to Alaska were defined in the previous section: the northeastern China Anthropogenic Emission (AE), the southeastern Siberia Biomass Burning Emission (BBE), and the Volcanic Emission (VE) from the Kamchatka/Aleutians (see Fig. 1). Fisher et al. (2011) found that East Asian anthropogenic sources were the largest contributors of sulphate during ARCTAS-A and ARCPAC (Aerosol, Radiation, and Cloud Processes affecting Arctic Climate – April 2008 – Alaska) (Brock et al., 2011) field missions, through transport in the free troposphere, followed closely by the European anthropogenic sources contributions at all altitudes during April 2008. The distance, to which highly polluted and possibly acidic air masses are transported, largely depends on the atmospheric circulation and conditions. Dry and wet depositions and chemical reactions play an important role on gas and aerosol lifetime. To assess the abundance and acidity of aerosols over Alaska in April 2008, one has to account for these factors.

In the current study, favorable periods of pollution transport are defined with the mean travel time from the three emission domains to the Alaska domain (see Fig. 1) during April 2008 using the Lagrangian Particle Dispersion Model (LPDM) FLEXPART

ACPD
13, 4331–4389, 2013

version 6 (Stohl et al., 1998, 2002). FLEXPART was driven by meteorological input data from the 6-hourly European Center for Medium-Range Weather Forecasts (ECMWF) analysis interleaved with operational forecasts every 3 h. In addition to classical advection, the LPDM includes turbulent diffusion, deposition and parameterizations of sub-grid scale convection. Results are discussed using forward trajectories to describe pollution transport to the Arctic. Ten-day forward trajectories were calculated with the FLEXPART model during the period of 22 March through 20 April 2008. The simulations were initialized each day at 12:00:00 UTC from 3 boxes in the AE domain and 3 boxes in the BBE domain. From the Kamchatka/Aleutians, five-day forward trajectories were calculated during the period of 27 March through 25 April 2008. The simulations were initialized each day at 12:00:00 UTC from 3 boxes located near the volcanoes of interest (VE). Box positions are shown using stars in Fig. 1. The height of all boxes was between 2000 and 2500 m. The starting point of a FLEXPART forward-trajectory is represented by a box with the following size: 0.5° lat. × 0.5° lon. × 500 m alt. For a selected box, 2000 particles are released during 60 min. The dispersion is described by the position of 5 clusters, each containing associated fractions of particles. Tables 1–3 give the travel time, the end point altitude/date and the fraction of particle reaching Alaska from the 3 boxes of the AE, BBE or VE domains, each day. From 22 March to 20 April 2008, only 4.9 % of particles leaving the AE domain reached Alaska against 8.1 % from the BBE domain. The average travel time of these trajectories to reach Alaska was about 6 ± 2 days (Tables 1 and 2). From 27 March to 25 April 2008, 32.2 % of particles leaving the 3 boxes of VE domain reached Alaska within 1 ± 1 days (Table 3). Considering the arrival date of particles from AE, BBE and VE domains to Alaska (Table 1), it is noted that an average of ∼ 10–12 %, ∼ 10–20 % and ∼ 37–50 % per day of particles emitted, respectively, from AE, BBE and VE domain boxes reached Alaska during periods A.1, B.1 and B.2, respectively. Almost no air mass emitted from the three domains reached Alaska during period A.2. These results, combined with the synoptic conditions described in the previous section, confirm that the low concentration of SO_2 recorded by OMI during the period A.2 is due to unfavorable weather conditions for the

ACPD
13, 4331–4389, 2013

transport of pollution into Alaska. The proximity of the source implies that the volcanic air masses have a larger impact on the Alaska domain compared to the air masses from eastern China/Russia. However, one has to consider that the air masses from eastern China/Russia pass generally over the volcanic zone before reaching Alaska, as shown by the weather conditions reported previously (Fig. 3).

The OMI SO_2 L2G data were used to assess qualitatively the transport of SO_2 in the free troposphere from anthropogenic and natural sources. Figure 6 shows the evolution and transport of the OMI total column density of SO_2 in the mid-troposphere (5–10 km) for ISDAC periods A.1, A.2, B.1 and B.2 (Fig. 2), over the Eastern part of Asia/Russia to Alaska. At first glance, a low concentration of SO_2 is recorded by OMI in mid-trosposphere above the Kamchatka/Aleutians during the period A.1 compared to the other three periods (Fig. 6a). More surprisingly, there is even a higher concentration of SO_2 above the VE domain during the period B.2 when a lower pollution rate is measured above the AE/BBE domains (Fig. 6d). These results suggest that volcanoes from Kamchatka/Aleutians were more active during periods A.2, B.1 and B.2 compared to period A.1. Therefore, the high concentration of SO_2 recorded over Alaska during the period B appears to be mostly of volcanic origin and therefore more acidic than during the period A.1. However, it is difficult to discriminate the SO_2 sources in the Alaska area knowing that the air masses can have been influenced by the three defined SO_2 sources. Also, one has to keep in mind the limits of OMI signal, which can be reduced by the chemical reaction of SO_2 into sulphate.

5 Polluted air masses – Arctic ice cloud interactions: case studies

5.1 ISDAC specific cases: overwiew and methodology

Two ice clouds representing each type of TICs (TIC-1/2A and TIC-2B) observed during the ISDAC campaign were investigated in detail in Jouan et al. (2012). The TIC-1/2A on Flight F9 was observed over the Barrow site on 1 April 2008 from 23:13:43 UTC to

ACPD
13, 4331–4389, 2013

23:45:43 UTC, corresponding to the relatively clean period A.1 identified in Sect. 2. The case of TIC-1/2A-F9 was sampled on a downdraft spiral in an area close to a warm front. The TIC-2B on Flight 21 was observed on 15 April 2008 from 00:55:26 UTC to 01:17:23 UTC, corresponding to the period B.1 that is heavily loaded with SO_2 as identified in Sect. 2. The case of TIC-2B-F21 was sampled on an updraft spiral in the center of a decaying low-pressure system.

In this section, the origin of the different observed air masses from which the TIC-1/2A-F9 and TIC-2B-F21 form is investigated in more details. Results are discussed examining the CALIPSO satellite tracks, which intersect the back-trajectories in the region away from the TICs layers observed by the aircraft and/or satellites to analyze aerosol occurrence and optical properties. The objective is to investigate in depth the link between TIC-2B formation and acidic aerosols using a lagrangian approach previously developed by de Villiers et al. (2010). It will be briefly described here. Both spiral profiles of flights F9 and F21 are divided in 13 boxes between 1 km and 7.5 km in altitude (500 m × 0.5° × 0.5°). The focus is put on the origin of air masses near the top of the cloud ($zt_{\text{TIC-1/2A-F9}}$ = 6.65 km and $zt_{\text{TIC-2B-F21}}$ = 6.75 km altitude from ISDAC airborne measurements – see Jouan et al., 2012), where most of the differences between the two clouds are found (Jouan et al., 2012). For a selected box, 2000 particles are released during 60 min. The particles dispersion is computed every 24 h during several days backward in time prior to the measurements and described by the averaged position of 5 clusters. The size of the clusters corresponds to the number of particles included in the cluster and the color to its altitude. The color of the mean trajectory of the particles represents the altitude of the ending point. Air mass trajectory estimates remain coherent when the 5 clusters (or at least the largest ones) stay close to each other (e.g. Fig. 7). CALIPSO tracks were selected when the time and horizontal position of the satellite overpass was less than 2 h and 200 km respectively from air mass positions estimates by the FLEXPART simulations (e.g. Fig. 8). The variational synergistic algorithm (Varcloud) developed by Delanoë and Hogan (2008) was used here to identify cloud and aerosol properties. This algorithm combines radar and

ACPD
13, 4331–4389, 2013

lidar observations to retrieve the ice water content (IWC), extinction and ice crystal effective radius (R_e) in regions of the cloud detected by both instruments. These operational products are called DARDAR (raDAR/liDAR) and are available at the data center ICARE (http://www.icare.fr) in France. More details on DARDAR can be found in Delanoë and Hogan (2008, 2010). Jouan et al. (2012) have demonstrated the ability of DARDAR to identify ice clouds of type TIC-1/2A and TIC-2B observed during the ISDAC campaign. Taking the A-Train overpass track closest in time and space from the studied ISDAC profiles F9 and F21 (discussed below), they quantified the mean values of T, β_{att}, Z, IWC and R_e retrieved from the Varcloud algorithm as a function of the normalized altitude of ice cloud layers within the TIC-1/2A and the TIC-2B. The ratio IWC/R_e is also calculated to get a representation of the ice particle number concentration in the cloud: mean values are presented in Table 4. The operational CALIOP aerosol data (version 3.01) is also used along the selected CALIPSO track. These products provide the optical properties of aerosol layers averaged every 5 km horizontally (Liu et al., 2009). Two additional criteria are considered: the layers detected only at a horizontal resolution of 80 km and an optical thickness at 532 nm over 0.03. These two conditions are needed to identify aerosol layers with low optical depths (de Villiers, 2010). All aerosol layers discussed in this section have a cloud-aerosol discrimination (CAD) greater than 90 %, which ensures that the detected layer by CALIOP contained aerosols (Eguchi et al., 2009).

5.2 1 April 2008 – TIC-1/2A-F9 ice cloud

On the TIC-1/2A-F9 profile, the transport pathway for the ensemble of 2000 particles released for two boxes: $B_{F9}1$ and $B_{F9}2$ are shown in Fig. 7. They are respectively characterized by their geographical coordinates in latitude, longitude and their altitude: $B_{F9}1$ (71.4° N; 156.3° W; 6.75 km) and $B_{F9}2$ (71.4° N; 156.3° W; 4.25 km). Air masses $B_{F9}1$ and $B_{F9}2$ originate 6 to 7 days before from eastern China/Siberia. They follow on average the tracks reports in Figs. 7a, b and 7c, d respectively. This synoptic pattern corresponds to the period A.1 and is described in Sect. 2, e.g. dominated by a direction

ACPD
13, 4331–4389, 2013

of flow from the western North Pacific Ocean into Alaska. Throughout the pathway from eastern China/Siberia to the Aleutians, air masses stay at an altitude ranging from 3 to 4 km until the last day, before rising over Alaska in their northward track. According to Tu et al. (2004), SO_2 transported at altitudes of 2–4 km from East Asia dominated the SO_2 distribution in the central Pacific. In our case, SO_2 concentrations appear to be smaller over northern Pacific (180° W and 40 to 60° N) early April than later (see Fig. 6). AMS data from the first two DC-8 ARCTAS flights (1 and 4 April 2008) were excluded due to apparent problems with the instrument (Fisher et al., 2011). Particles in the box $B_{F9}1$ more importantly rise (about 4 km) from 31 March to the observation time on 1 April at the top of the cloud around Barrow (see Fig. 7b), than particles in the $B_{F9}2$ box, located 2.5 km below. This upward motion spreads over a large distance ahead of the warm front.

Observed air masses ($B_{F9}1$ and $B_{F9}2$) of the TIC-1/2A-F9 pass just above the volcanoes of the Aleutians on 30 March (see Figs. 7 and 8). The daily volcano activity notifications of AVO reported weak volcanic tremor at Veniaminof at the end of March and a very weak thermal anomaly was detected at the summit of Cleveland on 30 March 2008. Air masses $B_{F9}1$ and $B_{F9}2$ intercept twice the CALIPSO/CloudSat track on 31 and 30 March 2008, respectively at 13:50 and 13:05:00 UTC (Fig. 8). Figure 9 shows the vertical profiles of DARDAR masks of these two selected track sections. On 31 March 2008, air masses $B_{F9}1$ and $B_{F9}2$ were located at 68° N just in front of an extended ice cloud (< 68° N) and above a mixed-phase cloud (65–72° N) (Fig. 9a). The slope of the ice cloud base between 64 and 68° N is associated with the arrival of the warm front over northern Alaska. One day before (30 March 2008), $B_{F9}1$ air mass was located just in front of a high-level ice cloud (< 48° N), whereas the $B_{F9}2$ air mass was located near the active Veniaminof volcano, in a cloudy area (identified $CL_{F9}1$ in Fig. 9b). Mean values of T, β_{att}, Z, IWC, R_e and IWC/R_e retrieved from the Varcloud algorithm along the normalized height of the extended ice cloud $CL_{F9}1$ (56.3–56.7° N) around the box $B_{F9}2$ are presented in Table 4. With similar temperatures and ice water contents on the first 2 km at the top of ice clouds, the averaged R_e of the $CL_{F9}1$

ACPD
13, 4331–4389, 2013

ice cloud is comparable to the averaged R_e of the TIC-1/2A-F9 ice cloud with a ratio IWC/R_e (index of ice crystals concentration) relatively high. $CL_{F9}1$ seems to belong to the category of TIC-1/2A with a high concentration of small ice crystals.

The CALIPSO/DARDAR mask independently reveals some aerosol layers near the $B_{F9}1$ and $B_{F9}2$ boxes between 65–74° N (identified $AL_{F9}1$ in Fig. 9a) in the mid-troposphere on 31 March and a wide aerosol layer (identified $AL_{F9}2$ in Fig. 9b) over southern Aleutians volcanoes between 41–52° N from 1 to 10 km in altitude on 30 March 2008. The mean attenuated backscatter coefficient at 532 nm (β_{att}), the mean volume depolarization ratio at 532 nm (δ_v) and the mean attenuated total color ratio (CR_{att}) for each aerosol layer are shown in Table 5. CALIPSO Level 2 aerosol layer data at 5 km resolution were used. The volume depolarization ratio (δ_v) in CALIOP products in aerosol layers is the ratio of the contributions in the backscattering direction of both molecules and particulates in a volume, of the cross-polarization to total signals. The attenuated total color ratio CR_{att} is derived from the attenuated backscatter ratio between 1064 nm and 532 nm. The relative variation in δ_v and CR_{att} go in the same direction as that of the particulate color ratio between 1064 nm and 532 nm (CR_p) and the particulate depolarization ratio at 532 nm (δ_p), but with a lower amplitude with decreasing optical thickness and values of fractions of aerosol accumulation mode. The volume depolarization ratio, δ_v as the attenuated total color ratio, CR_{att}, have the advantage of being less unstable than particulate parameters (δ_p, CR_P) when studying thin aerosol layers, e.g. when the particular contribution is low (de Villiers, 2010). Uncertainties in δ_v and CR_{att} are estimated to be about 10 % and 30 %, respectively (de Villiers, 2010).

The volume depolarization ratio (δ_v) associated with CR_{att} can qualitatively inform on the nature of the aerosol. δ_v is sensitive to particle shape. Spherical aerosols (e.g. haze and aqueous smoke particles) produce little or no changes in the polarization state of backscattered light, whereas non-spherical particles like dust or volcanic ashes can generate considerable depolarization (Mishchenko and Sassen, 1998; Atkinson et al., 2011). The relative increase in CR_{att} is related to the increase in particle size.

ACPD
13, 4331–4389, 2013

An increase of δ_v with particulate age during transport can occur as the aerosol loses its moisture coating, exposing the irregular aerosol surface (Sassen et al., 1989). Inversely, a decrease in δ_v associated to an increase in CR_{att} with particulate age during their transport can occur as the aerosol is coated with hydrophilic material and turned into such condensation nuclei causing sphering of the aerosol.

For both aerosol layers $AL_{F9}2$ and $AL_{F9}1$; β_{att} and CR_{att} do not vary much between 30 to 31 March 2008, with values of the order of β_{att} = 1.3–1.4 $Mm^{-1}\,sr^{-1}$ and CR_{att} = 0.26–0.23, respectively, while δ_v decreased more steeply from 7 to 4 % (Table 5).

Following Liu et al. (2009), one can broadly characterize each of CALIOP individual aerosol layers as "dust" when the volume depolarization ration (δ_v) is greater than 6 % or as "nondust" aerosol otherwise. The differences observed here remain small however, and this differentiation may be difficult. However, the back-trajectory analysis (Fig. 7a, b) associated to the higher value of the depolarization ratio (~ 7 %) (Table 5) of the $AL_{F9}2$ aerosols layer on 30 March 2008 suggest that the aerosol layer is composed of dust coming from dry regions of China and Mongolia (Gobi desert) probably mixed with anthropogenic pollution over Eastern China (AE). To a lesser extent some of the particles were previously in the area of biomass burning smoke (BBE) according to synoptic pattern in Fig. 3a. Tesche et al. (2009) and Giannakaki et al. (2012)'s approaches were used to separate mineral dust and non-dust (considered as anthropogenic particles) contributions based on CALIOP lidar observations. CALIPSO Level 2 aerosol profile data at 5 km resolution were used. Assuming that aerosols can be treated as two aerosol types externally mixed the particulate backscatter contribution of the first aerosol type ($\beta_{p,1}$) is obtained from the measured total particulate backscatter coefficient ($\beta_{p,t}$) by the following equation:

$$\beta_{p,1} = \beta_{p,t} \frac{(\delta_{p,t} - \delta_{p,2})(1 + \delta_{p,1})}{(\delta_{p,1} - \delta_{p,2})(1 + \delta_{p,t})} \quad (1)$$

where $\delta_{p,t}$, $\delta_{p,1}$ and $\delta_{p,2}$ are the observed total particulate depolarization ratio and the assumed particulate depolarization ratios of the two pure aerosol types, respectively.

ACPD
13, 4331–4389, 2013

The backscatter coefficient of the second aerosol type is given by the following equation

$$\beta_{p,2} = \beta_{p,t} - \beta_{p,1}. \quad (2)$$

The separation procedure, Eq. (1), was applied with dust aerosol representing aerosol type 1 and anthropogenic aerosol (or non-dust aerosol) representing aerosol type 2. A value $\delta_{p,1} = 0.35$ was considered for particulate depolarization ratio at 532 nm of Asian dust (Sugimoto et al., 2003; Shimizu et al., 2004). Non-dust particulate depolarization ratios $\delta_{p,2}$ can vary from 0.02 to 0.15 with an accumulation around 0.05 (Sugimoto et al., 2003; Tesche et al., 2009). The value $\delta_{p,2} = 0.05$ was considered for the aerosol type 2, as we suppose that transport over the ocean may induce larger moistening. Figure 10 shows the total particulate backscatter ($\beta_{p,t}$) and particulate extinction coefficient ($\alpha_{p,t}$) at 532 and 1064 nm, the total particulate depolarization ratio at 532 nm ($\delta_{p,t}$) and the profiles of the dust (yellow) and anthropogenic (red) backscatter coefficient separated by this analysis with the CALIOP scene classification algorithm of the aerosols layer $AL_{F9}2$. The separation procedure has revealed that the lower layer (< 3 km altitude), with a lower particulate depolarization ratio, is mixed while the middle and upper layer are consisting mainly in dust particles (Fig. 10d). CALIOP scene classification algorithm classifies a thin aerosol layer (1–2 km altitude) as polluted dust and the middle and upper aerosol layer as dust (Fig. 10e). Polluted dust is designed to account for episodes of dust mixed with biomass burning smoke and/or anthropogenic pollution, which is consistent with the results. The following aerosol layer $AL_{F9}1$, on 31 March, has a value $CR_{att} \sim 0.23$ and a value $\delta_v < 6\,\%$. CALIOP scene classification algorithm classifies the aerosol layer $AL_{F9}1$ as clean continental (Table 5). De Villiers (2010) notes that the CALIOP scene classification tends to define layers encountered after several days of transport as clean continental in the Arctic, while their analysis shows a connection with the Asian polluted sources. The decrease in δ_v associated to the slight decrease in CR_{att} between $AL_{F9}2$ in 30 March and $AL_{F9}1$ in 31 March can occur with the removal of the large particles by wet deposition just after the warm front

ACPD
13, 4331–4389, 2013

at the time of cloud dissipation of clouds (Fig. 9a) (Bègue et al., 2012). The relative humidity with respect to water (RH_{water}) inside the $AL_{F9}2$ (~ 29.8 %) was drier than $AL_{F9}1$ (~ 49.7 %) (Table 5), thus supporting this hypothesis.

These results show that air masses observed within the upper part of the TIC-1/2A-F9 ice cloud were mainly influenced by pure dust from dry regions of China and Mongolia with some mixture of anthropogenic pollution (AE) and possible biomass burning smoke (BBE). With a large proportion of desert dust compared to anthropogenic aerosols, added to a low activity of volcanoes from Kamchatka/Aleutians (Fig. 6a), air masses forming the TIC-1/2A-F9 can be classified as not acidic.

Based on synoptic meteorological analysis, air mass back trajectory studies using the FLEXPART model with surface lidar and balloon-borne aerosol measurements at the Fairbanks site, Atkinson et al. (2011) have shown that the first few days of April (1 April to midday 5 April 2008) were dominated by pristine clear conditions with a very low aerosol concentration. This is consistent with our findings.

5.3 15 April 2008 – TIC-2B-F21 ice cloud

On 15 April 2008 (TIC-2B-F21), the transport pathway for the ensemble of 2000 particles released for three boxes located at 6.75 km (hereafter $B_{F21}1$), 5.75 km (hereafter $B_{F21}2$) and 4.25 km (hereafter $B_{F21}3$) located as before over Barrow (71.5° N; 156.6° W) are shown in Fig. 11. Air masses forming the TIC-2B-F21 come from the Far Eastern Russia (Fig. 11a – $B_{F21}1$) and mainly from the Aleutians in a direct ($B_{F21}2$ in Fig. 11b) or a long transport path ($B_{F21}3$ in Fig. 11c). Due to the low-pressure system over Alaska, the air masses stay several days in the same area between 140° E–140° W and 45–75° N the 7 days prior to the observations. The $B_{F21}1$ air mass remains at high altitude (> 6 km) throughout its pathway, in a region (Far Eastern Russia) relatively clean according to the OMI observations. The $B_{F21}2$ air mass comes directly from the Aleutians with an upward motion from the PBL (altitude < 2 km) above the North Pacific Ocean 4 days before (on 12 April 2008) at 175° E longitude and 50° N latitude (see Fig. 11d), to ~ 5.75 km above the Bering Sea (3 days before) and the NSA (1–2 days before)

ACPD
13, 4331–4389, 2013

(Fig. 11c). $B_{F21}3$ air mass comes also from the Aleutians. It bypasses the low depression centered on Alaska, then passes over Western Canada and comes back to Barrow with a northwest component. There is a significant upward motion from the PBL (altitude < 3 km) to 4 km height above the Northwest Territories (2–3 days before) and the Beaufort Sea (1 day before) (see Fig. 11f). The OMI total SO_2 columns density at 5 km from 10 to 16 April 2008 (see Fig. 6c) show that the studied $B_{F21}2$ and $B_{F21}3$ air masses passed through heavily SO_2 (> 1.5 DU) polluted regions. Based on seismic and satellite data, the KVERT reported that weak ash-and-gas explosions may have occurred daily from the 10 to 14 April 2008 at Karymsky and Shiveluch (Kamchatka). $B_{F21}2$ and $B_{F21}3$ air masses are staying at low altitudes when passing over, and moving away from the Aleutian islands.

The back-trajectory of the $B_{F21}2$ air mass is further examined to identify the intercepts with CALIPSO and look at other ice clouds with DARDAR. The trajectory of this air mass crosses three times the CALIPSO satellite tracks in the three days preceding the observations (see Fig. 12). Figure 13a, b shows the vertical profiles of cloud properties retrieved by DARDAR of the track sections on 13 and 12 April 2008, respectively at 23:01:00 and 14:18:00 UTC. On 13 April 2008, $B_{F21}2$ air mass was located at 67° N inside an extended ice cloud between 58 and 72° N (identified as $CL_{F21}1$). On 12 April 2008, $B_{F21}2$ air mass was located further south at 58.5° N inside a second extended ice cloud between 50 and 63° N (identified as $CL_{F21}2$). Table 4 shows the mean values of T, β_{att}, Z, IWC, R_e and IWC/R_e along normalized height of extended ice cloud $CL_{F21}1$ (66.5–67° N) and $CL_{F21}2$ (58.0–58.5° N), around the $B_{F21}2$ box. For both extended ice cloud layers $CL_{F21}1$ and $CL_{F21}2$, the ratio IWC/R_e on the first 2 km at the top of ice clouds is as low as the TIC-2B-F21 ice clouds for an averaged R_e also relatively high. $CL_{F21}1$ and $CL_{F21}2$ belong to the category of TIC-2B with a low concentration of large ice crystals.

The CALIOP/DARDAR mask also reveals aerosol layers on either side of the ice cloud $CL_{F21}2$, between 44–51° N above the North Pacific Ocean ($AL_{F21}1$) and between 62–70° N just above the Bering Sea ($AL_{F21}2$) on 12 April 2008 (Fig. 13b).

ACPD
13, 4331–4389, 2013

$AL_{F21}1$ layer have low values of β_{att} and CR_{att} of about 1.7 $Mm^{-1}\,sr^{-1}$ and 0.31 with a volume depolarization ratio δ_v of about 5 ± 3 % (Table 5). CALIOP scene classification algorithm classifies the $AL_{F21}1$ layer as polluted dust (Table 5). A 10-day back-trajectory analysis (Fig. 14a) of one air mass box ($B_{F21}4$) in the $AL_{F21}1$ layer (47.4° N; 179.8° E; 3.75 km in Fig. 13b) reveals that the air mass come from dry regions of Gobi desert probably mixed with anthropogenic pollution over Eastern China (AE) without passing by the BBE domain. The analysis in terms of partitioning between dust and non-dust as done previously shows that dust contributes to around 50 % of scattering in the signal above 1 km (Fig. 15a and Table 5). The other aerosol layers $AL_{F21}2$ have lower δ_v (3 ± 3 %) and are classified as a continental clean air mass (Table 5). A 10-day back-trajectory analysis (Fig. 14b) of an air mass box ($B_{F21}5$) inside the $AL_{F21}2$ layer (64.6° N; 170.3° W; 3.75 km in Fig. 13b) reveal a contribution of biomass burning smoke.

The analysis in term of the aerosol layer lidar properties that intercept the $B_{F21}3$ air mass back-trajectory (Figs. 11e and 12) with CALIPSO reveals that aerosol layers along the $B_{F21}3$ (eastern part of Alaska) and $B_{F21}2$ (western part of Alaska) air mass back-trajectories seem to be relatively of the same composition. For example, the CALIPSO track section that intercepts the $B_{F21}3$ air mass back-trajectory on 10 April 2008 at ∼ 13:00:00 UTC (Fig. 12), reveals two aerosol layers between 44–60° N ($AL_{F21}3$ and $AL_{F21}4$ – Fig. 13c) above the Gulf of Alaska (Fig. 12). The analysis, in terms of partitioning between dust and non-dust as done previously shows a major (larger than 70 %) contribution of anthropogenic and/or biomass burning smoke scattering in the signal ($AL_{F21}3$ and $AL_{F21}4$) (Table 5).

Air masses observed in Alaska on 15 April 2008 appear to be influenced by a mixture of Asian dust (with a proportion of 50 % of anthropogenic pollution) and/or biomass burning smoke (BBE) (with a proportion of 70 % of smoke). No signature of fresh volcanic ash (e.g. higher values of δ_v due to the proximity) was found in the CALIOP data along back-trajectories of $B_{F21}2$ and $B_{F21}3$ air masses forming the TIC-2B-F21. Atkinson et al. (2011) show that, at the Fairbanks site, the second week of April (midday 5 to 17 April 2008) was dominated by Asian dust with some smoke probably resulting from

ACPD
13, 4331–4389, 2013

a flow from northern China and south-eastern Siberia, maintained by the presence of an anticyclone in the central North Pacific.

On 1 April 2008 Asian dust and biomass burning smoke follow a direction flow from the western North Pacific Ocean (Figs. 3a and 7a, c) to Alaska, providing opportunity to aerosol loss by wet deposition into the marine convective boundary layer (Tu et al., 2004; Atkinson et al., 2011). The synoptic pattern on 15 April 2008 promotes biomass burning smoke intrusion into Alaska following a fairly direct pathway from eastern Siberia to Alaska along the coast of Siberia/Kamchatka, the time spent over the ocean is significantly shorter (Figs. 3c and 14b). In addition, the decaying low-pressure system centered into Alaska brings westerly air masses (Asian dust + burning biomass smoke) into Alaska (Fig. 11e) during several days (Fig. 3c). Asian dust contribution as observed from the lidar signal analysis appears comparable in both cases, but the synoptic pattern observed in period B is favorable to the accumulation of pollutants from eastern China/Siberia into Alaska and may explain the higher accumulation of SO_2 concentrations above Alaska during the TIC-2B-F21 period compared to the TIC-1/2A-F9 period observed from the OMI data (Fig. 6a, c).

6 Discussion

OMI provides a unique perspective on variability of transport of SO_2 to the Arctic and can be used to identify long-range pollution tracks to the Arctic using FLEXPART forward trajectories as shown in previous section. Figure 16 shows another example of the transport and dispersion of high concentrations of anthropogenic pollution emitted from Beijing around 22 up ti the 26 March 2008. On 23 March polluted air masses moved along the east coast of Siberia. Then they crossed and spread over the Okhotsk Sea on 24 March to the south of the volcanic arc of the Aleutians/Kamchatka on 25 and 26 March. Figure 16b shows a 7-day forward trajectory initialized on 22 March at 12:00:00 UTC over Beijing in mid-troposphere at 7500 m altitude. There is a qualitatively good agreement between measured OMI total column density of SO_2 and

ACPD
13, 4331–4389, 2013

FLEXPART simulated forward trajectories, in the mid-troposphere from 22 to 26 March 2008. Forward trajectories from the sampled plume indicate that the plume did not travel poleward but rather to the west coast of USA.

Trajectory study with OMI satellite observations allow the identification of three favorable periods for the transport of air masses from northeastern China, southeastern Siberia and Kamchatka/Aleutians into Alaska during the ISDAC campaign: there are periods A.1 (27 March–2 April), B.1 (10–16 April) and B.2 (17–25 April). SO_2 OMI measurements showed that air masses reaching Alaska on 10 April 2008 until the end of the month (period B) seem more polluted (by a factor of 3 in SO_2 content) than during period A (27 March–9 April 2008). Nevertheless, most of the time, air masses coming from northeastern China and/or southeastern Siberia follow the same path and pass over the volcano area. For this reason, it becomes difficult to discriminate the SO_2 pollution sources. Polluted air masses from the northeastern China Anthropogenic Emission (AE) and the southeastern Siberia Biomass Burning Emission (BBE) are quite far from Alaska and have time to disperse over a large area. Figure 16 illustrates this phenomenon with a high concentration of SO_2 from AE and BBE sources that eventually disperse and lose in concentration along its path eastward. Moreover, several factors can change the OMI SO_2 signal: chemical reaction and dry deposition of SO_2 can reduce the signal; lofting of the plume (change of SO_2 vertical distribution) can enhance the signal; clouds can add to the OMI sensitivity to SO_2 above them but block SO_2 beneath. The overall result for this case, and very likely for other transport events in the lower troposphere, is that part of the SO_2 plume that can be detected over the source region would become less visible to OMI over downwind areas (Li et al., 2010).

Zhang et al. (2004) investigated the transport and chemical transformation of sulfur compounds over East Asia during the winter-spring season of 2001 using chemical and atmospheric models. Results have shown that the SO_2 and SO_4^{2-} concentrations show pronounced variations in time and space due to the interplay of chemical conversion, removal and transport processes. Analysis of model results has shown that the emission was the dominant term in regulating the SO_2 spatial distribution, while conversion

ACPD
13, 4331–4389, 2013

of SO_2 to SO_4^{2-} in the gas phase and the aqueous phase and wet removal were the primary factors that control SO_4^{2-} amounts. Simulations showed that 42 % sulfur compounds emitted in the model domain was transported out, while about 57 % (~ 35 % by wet removal processes) was deposited in the domain during the study period. It is thus difficult to quantify the change of the total SO_2 mass within the plume during transport, with OMI retrievals alone (Li et al., 2010).

Extensive chemical measurements from two airborne field experiments conducted in April 2008 over the North American Arctic (ARCTAS-A, Jacob et al., 2010, and ARCPAC, Brock et al., 2011) as well as surface seasonal observations at Arctic sites were performed during the International Polar Year (IPY). These measurements, combined with transport and coupled transport-chemistry models, provided unprecedented information on the sources of aerosols, including sulphate with their vertical distribution and confirm that the sulphate concentration over the NAA during the winter-spring 2008 period was related to a diversity of anthropogenic and natural sources (Brock et al., 2011; Fisher et al., 2011; Harrigan et al., 2011; Warneke et al., 2009, 2010). Air masses forming the TIC-1/2A-F9 as found in this study were composed of a high proportion of pure dust from dry regions of China and Mongolia with a low contribution of anthropogenic/smoke pollutants and SO_2, suggesting the absence of highly acidic ice nuclei. The air masses forming the TIC-2B-F21 as found in this study were composed of well mixed polluted dust with a relatively high contribution of anthropogenic/smoke pollutants (more than 70 %) and SO_2.

The level of acidity of the aerosols forming the TIC-2B-F21 ice cloud can been determined using in-situ measurements taken during the ARCPAC/ARCTAS Campaign and by examining the thermodynamic properties of the aerosol layer. The ARCPAC/ARCTAS projects overlapped in space and time with the Convair 580 aircraft from the ISDAC Campaign. The NASA ARCTAS P-3B and the NOAA ARCPAC WP-3-D aircrafts sampled the aerosol acidity near Barrow, on 15 April 2008, respectively, between 22:21:00–01:17:00 UTC and 00:25:00–02:12:00 UTC. An Aerosol Mass Spectrometer (AMS) (Dunlea et al., 2009) measuring submicron aerosol mass and composition as

ACPD
13, 4331–4389, 2013

a function of their size was used. These data are also within the precision of the ARCPAC AMS measurement (35 %). The observed aerosol acidity was defined by the mean neutralized fraction as $f = (NH_4^+)/(2(SO_4^{2-}) + (NO_3^-))$ with all concentrations in molar units (Fisher et al., 2011). On 15 April 2008, the average observed aerosol acidity in the area ±3° latitude and longitude coordinates around Barrow and above 2 km altitude gives low values of the order of 0.33 ± 0.15 (P-3B) and 0.46 ± 0.13 (WP-3-D), indicating the presence of highly acidic aerosols.

As explained previously, an increase of δ_v with particulate age during transport can occur as the aerosol loses its coating, exposing the irregular aerosol surface (Sassen et al., 1989). This is possible if an aerosol composed of ammonium sulfate crosses a dry area with a RH_{water} below its efflorescence point (~ 37 %). However, if the aerosol is coated with highly acidic conpound such as sulfuric acid, which is highly hygroscopic, it will not lose its moisture coating even at very low RH_{water}. In this situation, δ_v should remain unchanged. According to the results, aerosols layers ($AL_{F21}2$, $AL_{F21}3$ and $AL_{F21}4$) forming the TIC-2B are composed of a mixture of dust with anthropogenic and smoke pollutants and SO_2. One aerosol layer to the other, the δ_v remains unchanged (4–5 %) while CR_{att} and RH_{water} decrease from 0.31 to 0.24 and 50 to 34.1 %, respectively, below the efflorescence point of sulfate ammonium (Table 5). These results support the idea that air masses forming the TIC-2B-F21 were composed of acid-coated aerosols. Although no signature of volcanic ash was found in the CALIOP data, the contribution of volcanoes to the SO_2 accumulation in Alaska during period B is a reasonable hypothesis given the reported volcanic activities by KVERT.

7 Summary and conclusion

In this work, the temporal variability of Alaska-averaged SO_2 pollution from OMI satellite data, associated to the meteorological conditions during March–April 2008, was presented. Preliminary estimates of the SO_2 column amount were calculated based on an assumed SO_2 altitude of 5–10 km above Alaska. Two periods have been distinguished;

ACPD
13, 4331–4389, 2013

a relatively clean period (very little SO_2 concentration) from 27 March to 3 April 2008, and a more polluted period from the 10 to 25 April 2008 with a concentration of OMI SO_2 3 times higher than during the first period. Together with trajectory tools and OMI satellite data, the origins and the transport pathways of the SO_2 were identified during April 2008. The SO_2 emitted from the northeastern China Anthropogenic Emission and from the southeastern Siberia Biomass Burning Emission sources were generally transported to Alaska, passing over the Kamchatka/Aleutians volcanoes, in 5–7 days throughout the month of April. All of the three identified SO_2 pollution sources seem to have a direct influence on the SO_2 concentration into the North Slope of Alaska. The SO_2 distributions during the long-range transport were determined primarily by the atmospheric dynamics.

The origin of the air masses in which the ISDAC TIC-1/2A (1 April 2008) and TIC-2B (15 April 2008) were formed, was investigated to verify the hypothesis regarding the potential link between acidic aerosols and TIC-2B. Results are discussed by examining the CALIPSO satellite tracks, which intersects the back trajectories in the region away from the airborne measurements. Air masses observed within the upper part of the TIC-1/2A-F9 ice cloud were mainly influenced by a mixture of Asian dust with AE and possible BBE emissions. The separation procedure has revealed an aerosol layer (2 days before the ISDAC observations) slightly mixed with a higher proportion of pure dust aerosols. Added to a low activity of volcanoes from Kamchatka/Aleutians during this reported period, air masses forming the TIC-1/2A-F9 does not appear acidic. Air masses observed within the upper part of the TIC-2B-F21 ice cloud appear to be mainly influenced by an accumulation (due to specific weather conditions) of a mixture of Asian dust with BBE and possible VE emissions (due to important daily volcano activity, according to the KVERT report) into Alaska. The separation procedure has revealed aerosol layers (3 days before the ISDAC observations) well mixed with a higher proportion of anthropogenic and smoke aerosols. Airborne measurements revealed that aerosols were acidic around Barrow, near the sample ISDAC TIC-2B, on 15 April

ACPD
13, 4331–4389, 2013

2008. The thermodynamic properties associated to the CALIOP volume depolarization ratio also indicate that aerosols were highly acidic during the TIC-2B period.

These results and the analysis of aerosol moistening strongly support the hypothesis that acidic coating on IN are at the origin of the formation of TIC-2B. However, other studies are needed to confirm this hypothesis, in particular dedicated campaigns to investigate the link between acid-coated aerosols and TIC-2B clouds. The ice crystal growth rate in very cold conditions impinges on the precipitation efficiency, dehydration and radiation balance. A regional climate model evaluating the impact of the IN deactivation effect by acid coating on the cloud microstructure, precipitation and radiation have also been performed by Girard et al. (2012). Results show that acid coating on dust particles has an important effect on cloud microstructure, atmospheric dehydration, radiation and temperature over the Central Arctic, which is the coldest part of the Arctic.

Acknowledgements. This work was funded by the Natural Sciences and Engineering Research Council of Canada (NSERC), the Fonds Québécois de la Recherche sur la Nature et la Technologie (FQRNT) and the Centre National d'Etudes Spatiales (CNES). A. Stohl (NILU) and ECMWF are acknowledged for providing the FLEXPART model and the meteorological analyses. We also acknowledge the OMI mission scientists and associated NASA personnel for the production of the data used in this research effort. We thank the ICARE Data and Services Center (http://www.icare.univ-lille1.fr/) for providing access to the space-borne data used in this study. Gerard Ancellet and Raphaël Adam de Villiers are acknowledged for their work on FLEXPART modeling. We thank Steven Howell for providing acces to the ARCTAS AMS data.

The publication of this article is financed by CNRS-INSU.

ACPD
13, 4331–4389, 2013

References

ACIA: Impacts of a Warming Arctic: Arctic Climate Impact Assessment, Cambridge University Press, 1042, New York, USA, 2005.

Adams, P. J., Seinfeld, J. H., and Koch, D. M.: Global concentrations of tropospheric sulfate, nitrate, and ammonium aerosol simulated in a general circulation model, J. Geophys. Res., 104, 13791–13823, doi:10.1029/1999JD900083, 1999.

Atkinson, D. E., Sassen, K., Hayashi, M., Cahill, C. F., Shaw, G., Harrigan, D., and Fuelberg, H.: ARCTAS-A ground-based observational campaign and meteorological context, interior Alaska, April 2008, Atmos. Chem. Phys. Discuss., 11, 16499–16552, doi:10.5194/acpd-11-16499-2011, 2011.

Barrie, L. A. and Barrie M. J.: Chemical components of lower tropospheric aerosols in the high Arctic: six years of observations, J. Atmos. Chem., 11, 211–226, doi:10.1007/BF00118349, 1990.

Bègue, N., Tulet, P., Chaboureau, J. P., Roberts, G., Gomes, L., and Mallet, M.: Long-range transport of Saharan dust over northwestern Europe during EUCAARI 2008 campaign: evolution of dust optical properties by scavenging, J. Geophys. Res., 117, D17201, doi:10.1029/2012JD017611, 2012.

Blanchet, J.-P. and Girard, E.: Arctic greenhouse cooling, Nature, 371, 383, doi:10.1038/371383a, 1994.

Brock, C. A., Cozic, J., Bahreini, R., Froyd, K. D., Middlebrook, A. M., McComiskey, A., Brioude, J., Cooper, O. R., Stohl, A., Aikin, K. C., de Gouw, J. A., Fahey, D. W., Ferrare, R. A., Gao, R.-S., Gore, W., Holloway, J. S., Hübler, G., Jefferson, A., Lack, D. A., Lance, S., Moore, R. H., Murphy, D. M., Nenes, A., Novelli, P. C., Nowak, J. B., Ogren, J. A., Peischl, J., Pierce, R. B., Pilewskie, P., Quinn, P. K., Ryerson, T. B., Schmidt, K. S., Schwarz, J. P., Sodemann, H., Spackman, J. R., Stark, H., Thomson, D. S., Thornberry, T., Veres, P., Watts, L. A., Warneke, C., and Wollny, A. G.: Characteristics, sources, and transport of aerosols measured in spring 2008 during the aerosol, radiation, and cloud processes affecting Arctic Climate (ARCPAC) Project, Atmos. Chem. Phys., 11, 2423–2453, doi:10.5194/acp-11-2423-2011, 2011.

Carn, S. A., Krueger, A. J., Krotkov, N. A., Yang, K., and Levelt, P. F.: Sulfur dioxide emissions from Peruvian copper smelters detected by the Ozone Monitoring Instrument, Geophys. Res. Lett., 34, L09801, doi:10.1029/2006GL029020, 2007.

ACPD
13, 4331–4389, 2013

Chernoff, D. I. and Bertram, A. K.: Effects of sulfate coatings on the ice nucleation properties of a biological ice nucleus and several types of minerals, J. Geophys. Res., 115, D20205, doi:10.1029/2010JD014254, 2010.
Chin, M., Rood, R. B., Lin, S.-J., Müller, J.-F., and Thompson, A. M.: Atmospheric sulfur cycle simulated in the global model GOCART: model description and global properties, J. Geophys. Res., 105, 24671–24687, 2000.
Delanoë, J. and Hogan, R. J.: A variational scheme for retrieving ice cloud properties from combined radar, lidar and infrared radiometer, J. Geophys. Res., 113, D07204, doi:10.1029/2007JD009000, 2008.
Delanoë, J., and Hogan, R. J.: Combined CloudSat-CALIPSO-MODIS retrievals of the properties of ice clouds, J. Geophys. Res., 115, D00H29, doi:10.1029/2009JD012346, 2010.
Devasthale, A., Tjernström, M., Karlsson, K. G., Thomas, M. A., Jones, C., Sedlar, J., and Omar, A. H.: The vertical distribution of thin features over the Arctic analysed from CALIPSO observations – Part I: optically thin clouds, Tellus B, 63, 77–85, doi:10.1111/j.1600-0889.2010.00516.x, 2011.
de Villiers, R. A: Analyse des propriétés optiques des aérosols observés en Arctique pendant la campagne de printemps de l'API/POLARCAT, PhD Thesis, Université Pierre et Marie Curie, Paris, France, 2010.
de Villiers, R. A., Ancellet, G., Pelon, J., Quennehen, B., Schwarzenboeck, A., Gayet, J. F., and Law, K. S.: Airborne measurements of aerosol optical properties related to early spring transport of mid-latitude sources into the Arctic, Atmos. Chem. Phys., 10, 5011–5030, doi:10.5194/acp-10-5011-2010, 2010.
Dufresne, J.-L. and Bony, S.: An assessment of the primary sources of spread of global warming estimates from coupled atmosphere-ocean models, J. Climate, 21, 5135–5144,doi:10.1175/2008JCLI2239.1, 2008.
Dunlea, E. J., DeCarlo, P. F., Aiken, A. C., Kimmel, J. R., Peltier, R. E., Weber, R. J., Tomlinson, J., Collins, D. R., Shinozuka, Y., McNaughton, C. S., Howell, S. G., Clarke, A. D., Emmons, L. K., Apel, E. C., Pfister, G. G., van Donkelaar, A., Martin, R. V., Millet, D. B., Heald, C. L., and Jimenez, J. L.: Evolution of Asian aerosols during transpacific transport in INTEX-B, Atmos. Chem. Phys., 9, 7257–7287, doi:10.5194/acp-9-7257-2009, 2009.
Durant, A. J., Shaw, R. A., Rose, W. I., Mi, Y., and Ernst, G. G. J.: Ice nucleation and overseeding of ice in volcanic clouds, J. Geophys. Res., 113, D09206, doi:10.1029/2007JD009064, 2008.

ACPD
13, 4331–4389, 2013

Eastwood, M. L., Cremel, S., Wheeler, M., Murray, B. J., Girard, E., and Bertram, A. K.: Effects of sulfuric acid and ammonium sulfate coatings on the ice nucleation properties of kaolinite particles, Geophys. Res. Lett., 36, L02811, doi:10.1029/2008GL035997, 2009.
Eguchi, K., Uno, I., Yumimoto, K., Takemura, T., Shimizu, A., Sugimoto, N., and Liu, Z.: Trans-pacific dust transport: integrated analysis of NASA/CALIPSO and a global aerosol transport model, Atmos. Chem. Phys., 9, 3137–3145, doi:10.5194/acp-9-3137-2009, 2009.
Fisher, J. A., Jacoba, D. J., Wanga, Q., Bahreinib, R., Carougea, C. C., Cubisonb, M. J., Dibbe, J. E., Diehlf, T., Jimenezb, J. L., Leibenspergera, E. M., Meindersh, M. B. J., Pyei, H. O. T., Quinnj, P. K., Sharmak, S., Van Donkelaarl, A., and Yantoscaa, R. M.: Sources, distribution, and acidity of sulfate-ammonium aerosol in the Arctic in winter–spring, J. Atmos. Env., Biomass burning in Siberia 45, 7301–7318, doi:10.1016/j.atmosenv.2011.08.030, 2011.
Giannakaki, E., Balis, D., and Amiridis, V.: Vertical separation of aerosol types using of CALIPSO Level-2 products, Springer Atmospheric Sciences, Part 3, 981–986, doi:10.1007/978-3-642-29172-2_137, 2012.
Girard, E.: Étude d'un effet indirect des aérosols acides en Arctique: Le cycle de déshydratation, Ph. D. Thesis, McGill University, 311 pp., McGill University, Montréal, Qc, Canada, 1998.
Girard, E. and Blanchet, J. P.: Simulation of Arctic diamond dust and ice fog or thin stratus using an explicit aerosol-cloud-radiation model, J. Atmos. Sci., 58, 1199–1221, doi:10.1175/1520-0469(2001)058<1199:SOADDI>2.0.CO;2, 2001.
Grenier, P. and Blanchet, J. P.: Investigation of the sulphate-induced freezing inhibition effect from CloudSat and CALIPSO measurements, J. Geophys. Res., 115, D22205, doi:10.1029/2010JD013905, 2010.
Grenier, P., Blanchet, J. P., and Munoz-Alpizar, R.: Study of polar thin ice clouds and aerosols seen by CloudSat and CALIPSO during mid-winter 2007, J. Geophys. Res., 114, D09201, doi:10.1029/2008JD010927, 2009.
Harrigan, D. L., Fuelberg, H. E., Simpson, I. J., Blake, D. R., Carmichael, G. R., and Diskin, G. S.: Anthropogenic emissions during Arctas-A: mean transport characteristics and regional case studies, Atmos. Chem. Phys., 11, 8677–8701, doi:10.5194/acp-11-8677-2011, 2011.
He, H., Li, C., Loughner, C. P., Li, Z., Krotkov, N. A., Yang, K., Wang, L., Zheng, Y., Bao, X., Zhao, G., and Dickerson, R. R.: SO_2 over central China: measurements, nu-

ACPD
13, 4331–4389, 2013

merical simulations and the tropospheric sulfur budget, J. Geophys. Res., 117, D00K37, doi:10.1029/2011JD016473, 2012.
Hirdman, D., Burkhart, J. F., Sodemann, H., Eckhardt, S., Jefferson, A., Quinn, P. K., Sharma, S., Ström, J., and Stohl, A.: Long-term trends of black carbon and sulphate aerosol in the Arctic: changes in atmospheric transport and source region emissions, Atmos. Chem. Phys., 10, 9351–9368, doi:10.5194/acp-10-9351-2010, 2010.
Intrieri, J. M. and Shupe, M. D.: Characterization and radiative effects of diamond dust of the Western Arctic Ocean region, J. Climate, 17, 2953–2960, 2004.
IPCC: Climate Change 2007: Intergovernmental Panel of Climate Change, The Physical Science Basis, Cambridge University Press, 996 pp., Cambridge, United Kingdom and New York, NY, USA, 2007.
Jacob, D. J., Crawford, J. H., Maring, H., Clarke, A. D., Dibb, J. E., Emmons, L. K., Ferrare, R. A., Hostetler, C. A., Russell, P. B., Singh, H. B., Thompson, A. M., Shaw, G. E., McCauley, E., Pederson, J. R., and Fisher, J. A.: The Arctic Research of the Composition of the Troposphere from Aircraft and Satellites (ARCTAS) mission: design, execution, and first results, Atmos. Chem. Phys., 10, 5191–5212, doi:10.5194/acp-10-5191-2010, 2010.
Jouan, C., Girard, E., Pelon, J., Gultepe, I., Delanoë, J., and Blanchet, J. P.: Characterization of Arctic ice cloud properties observed during ISDAC, J. Geophys. Res., 117, 23, doi:10.1029/2012JD017889, 2012.
Khoder, M. J.: Atmospheric conversion of sulfur dioxide to particulate sulfate and nitrogen dioxide to particulate nitrate and gaseous nitric acid in an urban area, Chemosphere, 49, 675–684, 2002.
Krotkov, N. A., Carn, S. A., Krueger, A. J., Bhartia, P. K., and Yang, K.: Band residual difference algorithm for retrieval of SO_2 from the Aura Ozone Monitoring Instrument (OMI), IEEE T. Geosci. Remote Sens., 44, 1259–1266, doi:10.1109/TGRS.2005.861932, 2006.
Krotkov, N. A., McClure, B., Dickerson, R. R., Carn, S. A., Li, C., Bhartia, P. K., Yang, K., Krueger, A. J., Li, Z., Levelt, P. F., Chen, H., Wang, P., and Lu, D.: Validation of SO_2 retrievals from the Ozone Monitoring Instrument over NE China, J. Geophys. Res., 113, D16S40, doi:10.1029/2007JD008818, 2008.
Lampert, A., Ehrlich, A., Dörnbrack, A., Jourdan, O., Gayet, J.-F., Mioche, G., Shcherbakov, V., Ritter, C., and Wendisch, M.: Microphysical and radiative characterization of a subvisible midlevel Arctic ice cloud by airborne observations – a case study, Atmos. Chem. Phys., 9, 2647–2661, doi:10.5194/acp-9-2647-2009, 2009.

ACPD
13, 4331–4389, 2013

Law, K. S. and Stohl, A.: Arctic air pollution: origins and impacts, Science, 315, 1537–1540, doi:10.1126/science.1137695, 2007.
Lee, C., Martin, R. V., van Donkelaar, A., O'Byrne, G., Krotkov, N., Richter, A., Huey, L. G., and Holloway, J. S.: Retrieval of vertical columns of sulfur dioxide from SCIAMACHY and OMI: air mass factor algorithm development, validation, and error analysis, J. Geophys. Res., 114, D22303, doi:10.1029/2009JD012123, 2009.
Li, C., Krotkov, N. A., Dickerson, R. R., Li, Z., Yang, K., and Chin, M.: Transport and evolution of a pollution plume from northern China: a satellite-based case study, J. Geophys. Res., 115, D00K03, doi:10.1029/2009JD012245, 2010.
Liu, Z., Vaughan, M., Winker, D., Kittaka, C., Getzewich, B., Kuehn, R., Omar, A., Powell, K., Trepte, C., and Hostetlerd, C.: The CALIPSO lidar cloud and aerosol discrimination: version 2 algorithm and initial assessment of performance, J. Atmos. Ocean. Technol., 26, 1198–1213, doi:10.1175/2009JTECHA1229.1, 2009.
Lopez, T., Carn, S., Werner, C., Fee, D., Kelly, P., Doukas, M., Pfeffer, M., Webley, P., Cahill, C., Schneider, D.: Evaluation of redoubt volcano's sulfur dioxide emissions by the Ozone Monitoring Instrument, J. Volcanol. Geoth. Res., doi:10.1016/j.jvolgeores.2012.03.002, in press, 2013.
Lu, Z., Streets, D. G., Zhang, Q., Wang, S., Carmichael, G. R., Cheng, Y. F., Wei, C., Chin, M., Diehl, T., and Tan, Q.: Sulfur dioxide emissions in China and sulfur trends in East Asia since 2000, Atmos. Chem. Phys., 10, 6311–6331, doi:10.5194/acp-10-6311-2010, 2010.
McFarquhar, G. M., Ghan, S., Verlinde, J., Korolev, A., Strapp, J. W., Schmid, B., Tomlinson, J., Brooks, S. D., Collins, D. R., Cziczo, D., Dubey, M. K., Gultepe, I., Kok, G., Laskin, A., Lawson, P., Liu, P., Lubin, D., Mazzoleni, C., MacDonald, A. M., Wolde, M., Zelenyuk, A., Ferrare, R. A., Flynn, C., Shupe, M., Turner, D. D., Ovtchinnikov, M., Xie, S., and Liu, X.: The Indirect and Semi-Direct Aerosol Campaign (ISDAC), Bull. Am. Meteorol. Soc., 92, 183–201, doi:10.1175/2010BAMS2935.1, 2011.
Mishchenko, M. I. and Sassen, K.: Depolarization of lidar returns by small ice crystals: an application to contrails, Geophys. Res. Lett., 25, 309–312, 1998
Morrison, H., Curry, K. D., Shupe, M. D., and Zuidema P.: A new double-moment microphysics parameterization for application in cloud and climate models, Part II: Single-column modeling of Arctic clouds, J. Atmos. Sci., 62, 1678–1693, doi:10.1175/JAS3447.1, 2005.

ACPD
13, 4331–4389, 2013

Morrison, H., de Boer, G., Feingold, G., Harrington, J., Shupe M. D., and Sulia, K.: Resilience of persistent Arctic mixed-phase clouds, Nat. Geosci., 5, 11–17, doi:10.1038/NGEO1332, 2012.

Quinn, P. K., Shaw, G., Andrews, E., Dutton, E. G., Ruoho-Airola, T., and Gong, S. L.: Arctic haze: current trends and knowledge gaps, Tellus B, 59, 99–114, doi:10.1111/j.1600-0889.2006.00238.x, 2007.

Sassen, K., Zhao, H., and Yu, B. K.: Backscatter laser depolarization studies of simulated stratospheric aerosols: crystallized sulfuric acid droplets, Appl. Optics, 28, 3024–3029, 1989.

Seinfeld, J. H. and Pandis, S. N.: Atmospheric Chemistry and Physics: from Pollution to Climate Change, John Wiley & Sons, Inc., New York, 1326 pp., 1998.

Shimizu, A., Sugimoto, N., Matsui, I., Arao, K., Uno, I., Murayama, T., Kagawa, N., Aoki, K., Uchiyama, A., and Yamazaki, A.: Continuous observations of Asian dust and other aerosols by polarization lidars in China and Japan during ACE-Asia, J. Geophys. Res., 109, D19S17, doi:10.1029/2002JD003253, 2004.

Shupe, M. D.: Clouds at Arctic atmospheric observatories, Part II: Thermodynamic phase characteristics, J. Appl. Meteor. Clim., 50, 645–661, doi:10.1175/2010JAMC2468.1, 2011.

Shupe, M. D. and Intrieri, J. M.: Cloud radiative forcing of the Arctic surface: the influence of cloud properties, surface albedo, and solar zenith angle, J. Climate, 17, 616–628, doi:10.1175/1520-0442(2004)017<0616:CRFOTA>2.0.CO;2, 2004.

Spinei, E., Carn, S. A., Krotkov, N. A., Mount, G. H., Yang, K., and Krueger, A.: Validation of ozone monitoring instrument SO_2 measurements in the Okmok volcanic cloud over Pullman, WA, July 2008, J. Geophys. Res., 115, D00L08, doi:10.1029/2009JD013492, 2010.

Stohl, A., Hittenberger, M., and Wotawa, G.: Validation of the Lagrangian particle dispersion model FLEXPART against large scale tracer experiment data, Atmos. Environ., 32, 4245–4264, 1998.

Stohl, A., Eckhardt, S., Forster, C., James, P., Spichtinger, N., and Seibert, P.: A replacement for simple back trajectory calculations in the interpretation of atmospheric trace substance measurements, Atmos. Environ., 36, 4635–4648, 2002.

Sugimoto, N., Uno, I., Nishikawa, M., Shimizu, A., Matsui, I., Dong, X., Chen, Y., and Quan, H.: Record heavy Asian dust in Beijing in 2002: observations and model analysis of recent events, Geophys. Res. Lett., 30, 1640, doi:10.1029/2002GL016349, 2003.

Sullivan, R. C., Petters, M. D., DeMott, P. J., Kreidenweis, S. M., Wex, H., Niedermeier, D., Hartmann, S., Clauss, T., Stratmann, F., Reitz, P., Schneider, J., and Sierau, B.: Irreversible loss

ACPD
13, 4331–4389, 2013

of ice nucleation active sites in mineral dust particles caused by sulphuric acid condensation, Atmos. Chem. Phys., 10, 11471–11487, doi:10.5194/acp-10-11471-2010, 2010.
Tesche, M., Ansmann, A., Müller, D., Althausen, D., Engelmann, R., Freudenthaler, V., and Groß, S.: Vertically resolved separation of dust and smoke over Cape Verde using multi-wavelength Raman and polarization lidars during Saharan Mineral Dust Experiment 2008, J. Geophys. Res., 114, D13202, doi:10.1029/2009JD011862, 2009.
Tu, F. H., Thornton, D. C., Bandy, A. R., Carmichael, G. R., Tang, Y., Thornhill, K. L., Sachse, G. W., and Blake, D. R.: Long-range transport of sulfur dioxide in the central Pacific, J. Geophys. Res., 109, D15S08, doi:10.1029/2003JD004309, 2004.
Uno I., Eguchi, K., Yumimoto, K., Takemura, T., Shimizu, A., Uematsu, M., Liu, Z., Wang, Z., Hara, Y., and Sugimoto, N.: Asian dust transported one full circle around the globe, Nat. Geosci., 2, 557–560, doi:10.1038/NGEO583, 2009.
Uttal, T., Curry, J. A., McPhee, M. G., Perovich, D. K., Moritz, R. E., Maslanik, J. A., Guest, P. S., Stern, H. L., Moore, J. A., Turenne, R., Heiberg, A., Serreze, M. C., Wylie, D. P., Persson, P. O. G., Paulson, C. A., Halle, C., Morison, J. H., Wheeler, P. A., Makshtas, A., Welch, H., Shupe, M. D., Intrieri, J. M., Stamnes, K., Lindsey, R. W., Pinkel, R., Pegau, W. S., Stanton, T. P., and Grenfeld, T. C.: Surface heat budget of the Arctic ocean, Bull. Am. Meteorol. Soc., 83, 255–275, doi:10.1175/1520-0477(2002)083<0255:SHBOTA>2.3.CO;2, 2002.
Warneke C., Bahreini, R., Brioude, J., Brock, C. A., De Gouw, J. A., Fahey, D. W., Froyd, K. D., Holloway, J. S., Middlebrook, A., Miller, L., Montzka, S., Murphy, D. M., Peischl, J., Ryerson, T. B., Schwarz, J. P., Spackman, J. R., and Veres, P.: Biomass burning in Siberia and Kazakhstan as the main source for Arctic Haze over the Alaskan Arctic in April 2008, Geophys. Res. Lett. 36, L02813, doi:10.1029/2008GL036194, 2009.
Warneke, C., Froyd, K. D., Brioude, J., Bahreini, R., Brock, C. A., Cozic, A., de Gouw, J. A., Fahey, D. W., Ferrare, R. A., Holloway, J. S., Middlebrook, A. M., Miller, L., Montzka, S., Schwarz, J. P., Sodemann, H., Spackman, J. R., and Stohl, A.: An important contribution to springtime Arctic aerosol from biomass burning in Russia, Geophys. Res. Lett., 37, L01801, doi:10.1029/2009GL041816, 2010.
Yalcin, K., Wake, C. P., and Germani, M.: A 100-yr record of North Pacific volcanism in an ice core from Eclipse Icefield, Yukon Territory, Canada, J. Geophys. Res., 108, 4012, doi:10.1029/2002JD002449, 2002.

ACPD
13, 4331–4389, 2013

Yang, K., Krotkov, N. A., Krueger, A. J., Carn, S. A., Bhartia, P. K., and Levelt, P. F.: Retrieval of large volcanic SO_2 columns from the Aura Ozone Monitoring Instrument: comparison and limitations, J. Geophys. Res., 112, D24S43, doi:10.1029/2007JD008825, 2007.

Zhang, M., Uno, I., Yoshida, Y., Xu, Y., Wang, Z., Akimoto, H., Bates, T., Quinn, T., Bandy, A., and Blomquist, B.: Transport and transformation of sulfur compounds over East Asia during the TRACE-P and ACE-Asia campaigns, Atmos. Environ., 38, 6947–6959, doi:10.1016/j.atmosenv.2004.02.073, 2004.

ACPD
13, 4331–4389, 2013

Table 1. List of days on which FLEXPART simulated 10-day froward trajectories from the AE domain reached the Alaskan domain, with the particles' fraction, travel time, altitude and date of arrival associated, from the end of March to the end of April 2008.

North-eastern China Anthopogenic Emission			Total number of trajectories reaching alaska = 4.3 %	
Initial Date y/m/d	Trajectories Nb	Travel Time Days	Arrival Altitude km	Arrival Date y/m/d
08/03/22	1	9	4.9	08/03/31
08/03/23	3	8 ± 1	5.67 ± 1.43	08/03/31
08/03/25	5	7 ± 2	5.76 ± 0.03	08/04/01
08/03/26	4	7 ± 2	5.94 ± 0.06	08/04/02
08/03/27	3	4	5.48 ± 2.11	08/03/31
08/03/28	1	6	3.4	08/04/03
08/03/29	1	4	7.26	08/04/02
08/03/30	3	4 ± 1	6.24 ± 0.10	08/04/03
08/03/31	1	4	7.26	08/04/04
08/04/05	1	6	2.94	08/04/11
08/04/06	2	8	2.9 ± 0.01	08/04/15
08/04/08	1	5	3.9	08/04/13
08/04/09	3	5 ± 3	5.78 ± 1.69	08/04/14
08/04/11	6	5 ± 2	4.42 ± 1.32	08/04/16
08/04/12	2	8 ± 1	6.95 ± 4.13	08/04/20
08/04/13	1	3	4.9	08/04/16
08/04/14	6	6 ± 1	9.03 ± 1.59	08/04/20
08/04/15	1	9	4.46	08/04/24
08/04/16	2	6 ± 2	7.28 ± 2.99	08/04/22
08/04/17	4	9	6.8	08/04/26
08/04/18	1	6	6.46	08/04/24
08/04/20	7	5 ± 2	6.66 ± 1.57	08/04/25
	Mean	6.03 ± 2.08	6.04 ± 1.93	

ACPD
13, 4331–4389, 2013

Table 2. List of days on which FLEXPART simulated 10-day froward trajectories from the BBE domain reached the Alaskan domain, with the particles' fraction, travel time, altitude and date of arrival associated, from the end of March to the end of April 2008.

South-eastern Russia Biomass Burning Emission			Total number of trajectories reaching alaska = 13.1 %	
Initial Date y/m/d	Trajectories Nb	Travel Time Days	Arrival Altitude km	Arrival Date y/m/d
08/03/23	1	8	4.72	08/03/31
08/03/24	1	7	4.42	08/03/31
08/03/25	2	8 ± 1	5.29 ± 0.99	08/04/02
08/03/26	2	4 ± 1	4.63 ± 0.39	08/03/30
08/04/02	1	8	4.15	08/04/10
08/04/03	2	8 ± 1	3.30 ± 1.45	08/04/11
08/04/06	2	6 ± 1	3.45 ± 0.82	08/04/12
08/04/07	1	9	3.16	08/04/16
08/04/08	4	5 ± 1	3.04 ± 8.46	08/04/13
08/04/09	1	8	3.21	08/04/17
08/04/11	1	8	2.72	08/04/19
08/04/12	6	6 ± 1	3.33 ± 1.79	08/04/18
08/04/13	5	4 ± 1	4.65 ± 0.27	08/04/17
08/04/14	4	2 ± 1	5.29 ± 0.20	08/04/16
08/04/16	2	8 ± 1	5.10 ± 0.47	08/04/14
08/04/17	1	8	4.48	08/04/25
08/04/18	3	4 ± 1	7.30 ± 1.37	08/04/22
	Mean	5.67 ± 2.25	4.33 ± 1.47	

ACPD
13, 4331–4389, 2013

Table 3. List of days on which FLEXPART simulated 5-day forward-trajecotires from the VE domain reached the Alaskan domain, with the particles' fraction, travel time, altitude and date of arrival associated, from the end of March to the end of April 2008.

Volcanic Emission			Total number of trajectories reaching alaska = 32.3 %	
Initial Date y/m/d	Trajectories Nb	Travel Time Days	Arrival Altitude km	Arrival Date y/m/d
08/03/27	3	2 ± 1	2.08 ± 0.07	08/03/29
08/03/28	10	1	2.87 ± 1.09	08/03/29
08/03/29	10	0	2.76 ± 0.40	08/03/29
08/03/30	10	1	1.95 ± 0.61	08/03/31
08/03/31	10	1 ± 1	2.48 ± 0.22	08/04/01
08/04/01	9	2 ± 1	1.79 ± 0.83	08/04/03
08/04/02	5	0	3.04 ± 0.26	08/04/02
08/04/03	10	1 ± 1	2.70 ± 0.28	08/04/04
08/04/09	6	2 ± 1	2.80 ± 1.18	08/04/11
08/04/11	3	1 ± 1	4.07 ± 0.77	08/04/12
08/04/14	3	3 ± 1	1.85 ± 0.14	08/04/17
08/04/15	9	2 ± 2	2.51 ± 1.12	08/04/17
08/04/16	10	1 ± 1	1.19 ± 0.40	08/04/17
08/04/17	6	0	2.75 ± 0.40	08/04/17
08/04/18	10	0	2.46 ± 0.16	08/04/18
08/04/19	5	0	2.18 ± 0.29	08/04/19
08/04/22	6	1 ± 1	2.48 ± 0.62	08/04/23
08/04/23	5	0	2.29 ± 0.22	08/04/23
08/04/24	10	1	3.13 ± 0.43	08/04/25
08/04/25	5	0	3.73 ± 0.80	08/04/25
	Mean	0.89 ± 1.06	2.50 ± 0.84	

ACPD
13, 4331–4389, 2013

Table 4. T, β, Z, IWC, R_e and IWC/R_e from VarCloud Algorithm of different ice cloud layers defined in Figs. 9 and 12 with their associated standard deviation, according to the normalized altitude.

Cloud Layer (CL)	z/zt	T (°C)	β_{att} ($\log_{10}$ sr^{-1} m^{-1})	Z (dBZ)	IWC (10^{-3} g m^{-3})	R_e (µm)	IWC/R_e (g m^{-4})
TIC-1/2A–F9	[1.0–0.9]	−44.0 ± 2.0	−5.31 ± 0.20	−30.0 ± 2.3	14.31 ± 5.41	27.6 ± 1.2	514.8 ± 191.1
Lat: 71.0–71.5° N	[0.9–0.8]	−38.1 ± 1.9	−5.25 ± 0.09	−22.7 ± 1.9	23.04 ± 4.77	33.6 ± 2.5	690.2 ± 87.5
Zt = 7.60 km	[0.8–0.7]	−32.1 ± 2.0	−5.45 ± 0.06	−16.7 ± 2.0	25.34 ± 1.40	40.7 ± 2.2	616.2 ± 63.5
	[0.7–0.6]	−26.3 ± 1.8	−5.45 ± 0.05	−12.2 ± 1.2	28.14 ± 2.55	46.6 ± 1.9	580.6 ± 24.4
$CL_{F9}1$	[1.0–0.9]	−55.1 ± 2.2	−5.09 ± 0.34	−27.9 ± 3.1	12.4 ± 5.9	30.0 ± 2.0	400.2 ± 183.2
Lat: 56.3–56.7° N	[0.9–0.8]	−47.6 ± 2.5	−5.55 ± 0.37	−22.1 ± 0.7	11.6 ± 3.9	35.5 ± 1.5	331.9 ± 130.5
Zt = 9.72 km	[0.8–0.7]	−39.8 ± 2.5	−5.48 ± 0.28	−15.3 ± 4.6	21.5 ± 12.0	42.8 ± 3.2	479.3 ± 239.0
	[0.7–0.6]	−31.9 ± 2.5	−5.90 ± 0.47	−9.1 ± 1.0	64.8 ± 10.4	51.2 ± 2.3	1148.3 ± 93.7
TIC-2–F21	[1.0–0.9]	−41.3 ± 0.6	−5.69 ± 0.11	−30.0 ± 2.0	3.81 ± 0.93	36.8 ± 1.0	104.3 ± 25.6
Lat: 71.0–71.5° N	[0.9–0.8]	−38.8 ± 1.1	−5.59 ± 0.10	−21.6 ± 3.5	6.09 ± 2.15	41.7 ± 2.4	143.0 ± 39.0
Zt = 5.94 km	[0.8–0.7]	−34.7 ± 1.5	−5.31 ± 0.09	−12.8 ± 1.8	15.70 ± 2.75	49.4 ± 2.0	310.5 ± 45.2
	[0.7–0.6]	−30.6 ± 1.2	−5.46 ± 0.14	−14.0 ± 2.3	12.08 ± 3.33	49.4 ± 1.8	238.7 ± 59.0
$CL_{F21}1$	[1.0–0.9]	−48.2 ± 2.2	−5.81 ± 0.14	−31.3 ± 1.5	3.07 ± 0.78	33.2 ± 1.2	91.5 ± 20.5
Lat: 66.5–67.0° N	[0.9–0.8]	−40.9 ± 2.3	−5.67 ± 0.08	−29.1 ± 0.9	3.91 ± 0.31	36.2 ± 0.8	108.8 ± 9.6
Zt = 7.62 km	[0.8–0.7]	−34.1 ± 2.0	−5.48 ± 0.27	−22.1 ± 5.7	6.71 ± 3.95	41.8 ± 3.7	155.4 ± 75.4
	[0.7–0.6]	−28.6 ± 1.5	−5.16 ± 0.20	−11.4 ± 1.8	22.66 ± 3.49	50.9 ± 1.1	440.5 ± 62.6
$CL_{F21}2$	[1.0–0.9]	−54.5 ± 2.4	−5.93 ± 0.23	−30.4 ± 1.7	2.47 ± 0.86	31.7 ± 2.2	76.1 ± 24.2
Lat: 58.0–58.5° N	[0.9–0.8]	−46.0 ± 2.6	−5.50 ± 0.09	−23.6 ± 2.9	5.11 ± 1.00	38.2 ± 2.2	133.6 ± 17.4
Zt = 10.44 km	[0.8–0.7]	−37.9 ± 2.5	−5.49 ± 0.07	−18.4 ± 0.8	6.35 ± 0.35	44.4 ± 2.3	144.2 ± 14.6
	[0.7–0.6]	−30.3 ± 2.1	−5.51 ± 0.09	−11.1 ± 3.8	10.83 ± 4.71	58.7 ± 6.4	178.1 ± 57.4

ACPD
13, 4331–4389, 2013

Table 5. Aerosol layer characteristics defined in previous Figures from the CALIOP lidar observations.

Aerosol Layer	$AL_{F9}1$	$AL_{F9}2$	$AL_{F21}1$	$AL_{F21}2$	$AL_{F21}3$	$AL_{F21}4$
Date (m/d)	08/03/31	08/03/30	08/04/12	08/04/12	08/04/10	08/04/10
Time (UTC)	13:49–14:29	13:11–13:40	14:19–14:48	14:18	12:53–13:21	12:51–13:23
Start Lat/Lon (°)	65.0/−163.8	41.3/174.4	44.5/178.7	62.0/−178.3	42.2/−160.4	52.0/−156.1
End Lat/Lon (°)	71.0/−156.7	51.3/170.7	51.0/−178.7	69.2/−165.3	52.0/−156.6	59.0/−152.9
Z_{min}–Z_{max} (km)	2.3–7.3	1–11	1.4–8.7	1.4–7	2–7.5	2.5–8.5
$\beta_{532,att}$ ($Mm^{-1}\,sr^{-1}$)	1.4 ± 0.3	1.3 ± 0.4	1.7 ± 0.5	1.7 ± 0.4	1.5 ± 0.3	1.5 ± 0.3
CR_{att}	0.23 ± 0.38	0.26 ± 0.23	0.31 ± 0.21	0.24 ± 0.17	0.27 ± 0.17	0.24 ± 0.15
δ_v	4 ± 4	7 ± 4	5 ± 3	3 ± 3	5 ± 3	4 ± 3
CFC	C.C	D	P.D	C.C	P.D	P.D
$\beta_{532,p,t}$ ($Mm^{-1}\,sr^{-1}$)	0.44 ± 0.15	0.52 ± 0.29	0.50 ± 0.30	0.60 ± 0.32	0.61 ± 0.18	0.65 ± 0.28
$\beta_{532,p,1}$ = Dust	0.14 ± 0.13	0.32 ± 0.17	0.27 ± 0.18	0.09 ± 0.13	0.18 ± 0.07	0.15 ± 0.09
$\beta_{532,p,2}$ = Pollutant	0.27 ± 0.19	0.21 ± 0.25	0.24 ± 0.24	0.51 ± 0.39	0.43 ± 0.17	0.50 ± 0.27
$\alpha_{p,t}$ (km^{-1})	0.023 ± 0.012	0.021 ± 0.012	0.023 ± 0.014	0.024 ± 0.012	0.034 ± 0.01	0.038 ± 0.02
$\delta_{p,t}$ (%)	16 ± 13	24 ± 10	23 ± 15	10 ± 5	13 ± 4	12 ± 7
RH_{Water} (%)	49.7 ± 15.8	29.8 ± 18.5	59.0 ± 17.5	46.0 ± 24.9	38.0 ± 18.2	34.1 ± 14.2

ACPD
13, 4331–4389, 2013

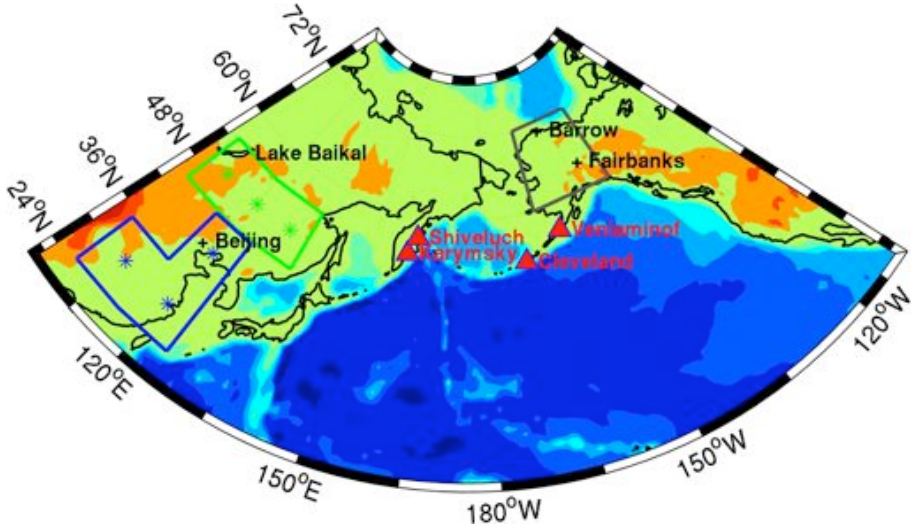

Fig. 1. Study Area: Alaska (195–220° W; 60–72° N – in gray) and Domains of potential SO_2 emission to Alaska used for the FLEXPART simulations; the north-eastern China Anthropogenic Emission (AE – in blue); the south-eastern Russia Biomass Burning Emission (BBE – in green) and the Volcanic Emission (VE – in red) from the Kamchatka Peninsula and Aleutians. In red triangle, the position and name of active volcanoes during April 2008.

ACPD
13, 4331–4389, 2013

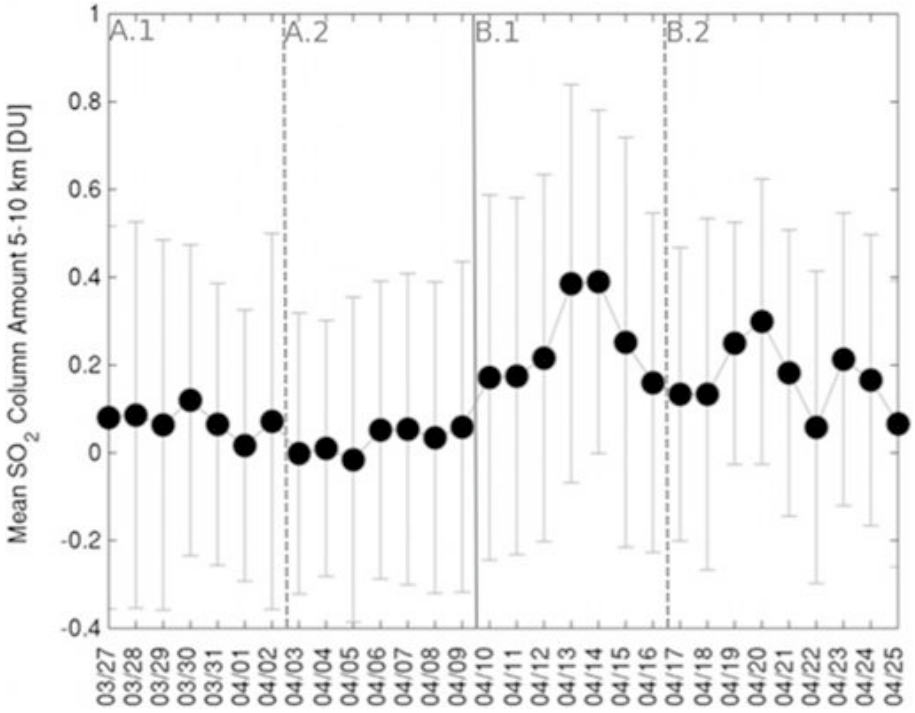

Fig. 2. Daily variability of the area-averaged SO_2 total column above Alaska (Fig. 1) from 27 March to 25 April 2008 based on an assumed SO_2 altitude between 5 to 10 km (TRM OMI L2G SO_2 products). Vertical lines represents the standard deviation. Results should be considered preliminary estimate.

ACPD
13, 4331–4389, 2013

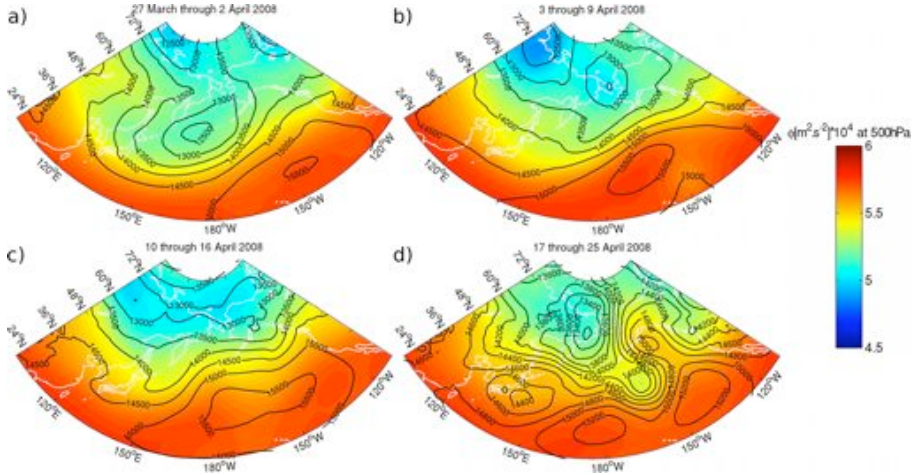

Fig. 3. Mean geopotential ($m^2\,s^{-2}$) at 850 hPa (contour) and 500 hPa (colorbar) from 27 March to 2 April **(a)**, 3 to 9 April **(b)**, 10 to 16 April **(c)** and 17 to 25 April **(d)** 2008.

ACPD
13, 4331–4389, 2013

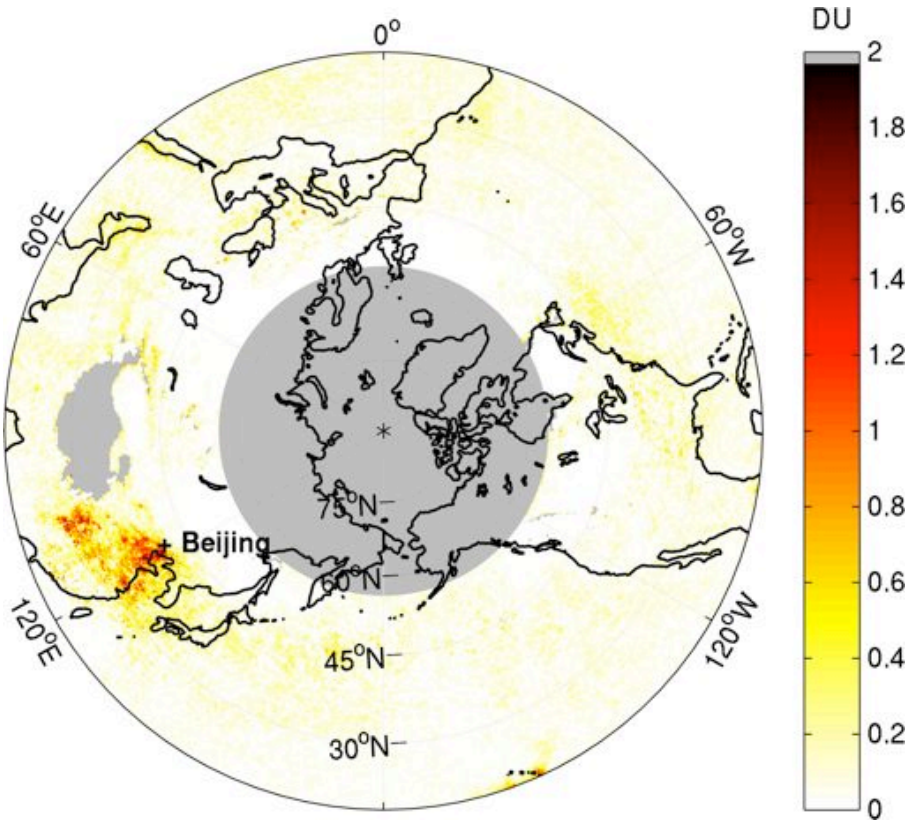

Fig. 4. Monthly mean SO_2 total column based on an assumed SO_2 altitude below 2 km (PBL OMI L3 SO_2 products) over the Northern Hemisphere in April 2008.

ACPD
13, 4331–4389, 2013

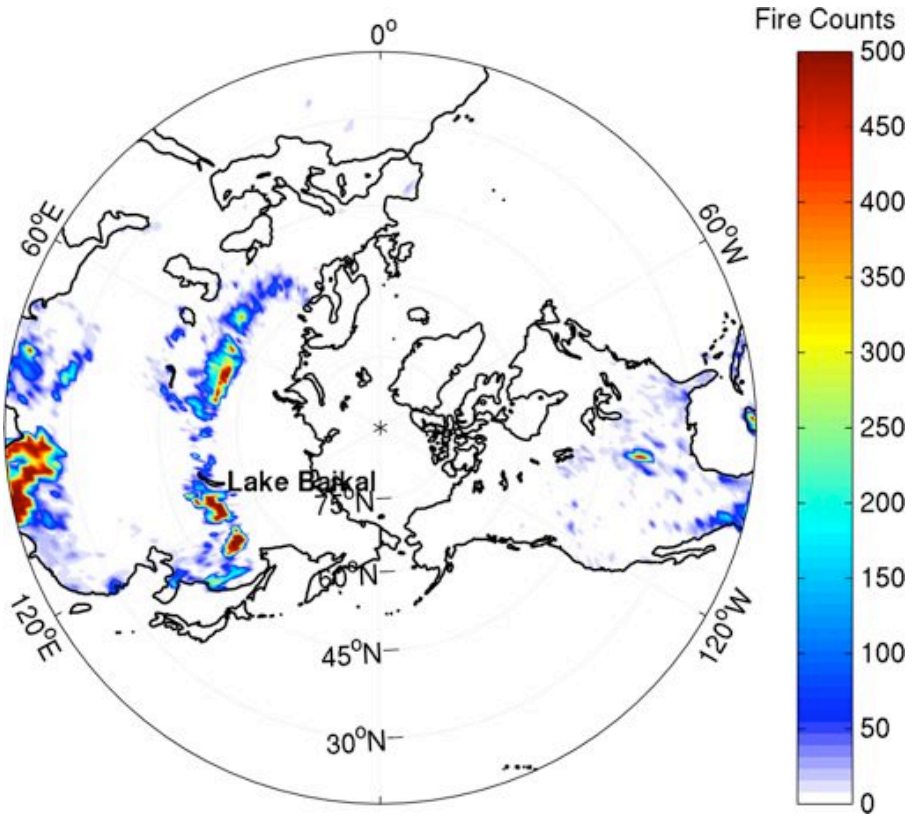

Fig. 5. Fire counts on April 2008 from the MODIS Aqua satellite instrument cloud- and overpass-corrected, over the Northern Hemisphere.

ACPD
13, 4331–4389, 2013

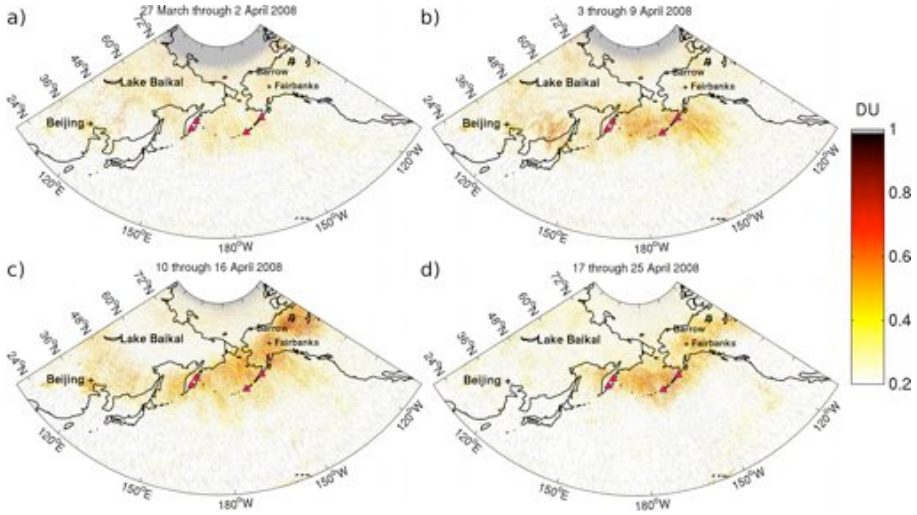

Fig. 6. Mean SO_2 total column based on an assumed SO_2 altitude between 5 to 10 km (TRM OMI L2G SO_2 products) from 27 March to 2 April **(a)**, 3 to 9 April **(b)**, 10 to 6 April **(c)** and 17 to 25 April **(d)** 2008.

ACPD
13, 4331–4389, 2013

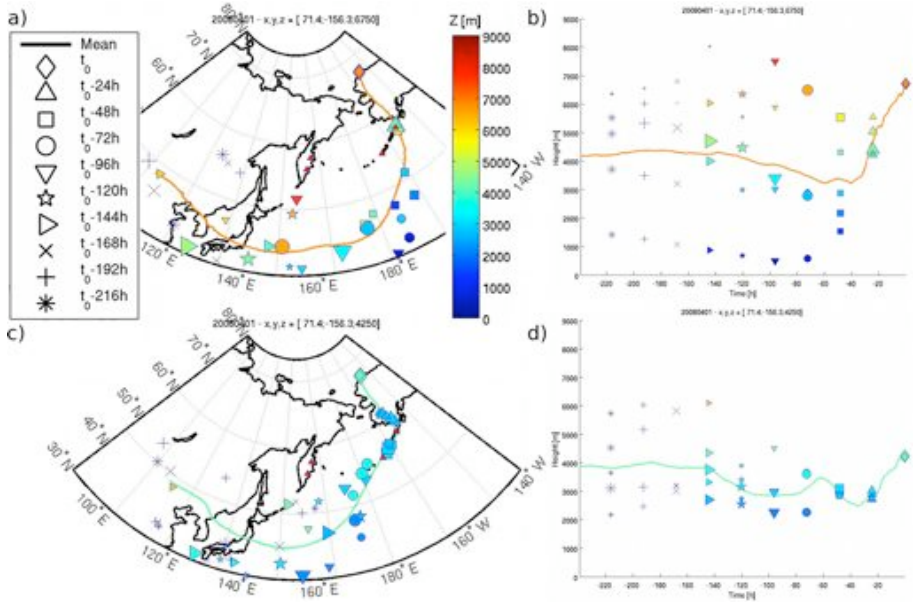

Fig. 7. 10-days backward-trajectories from FLEXPART simulations initialized on 1 April 2008 at 23:14:00 for boxes located at 71.4° N, 156.3° W at 6.75 km heigth ($B_{F9}1$) **(a, b)** and 4.25 km height ($B_{F9}2$) **(c, d)**. Clusters of particles are represented every 24 h from the beginning of the simulation. The colorbar represents the altitude of cluster in meters. Particles are released during one hour.

ACPD
13, 4331–4389, 2013

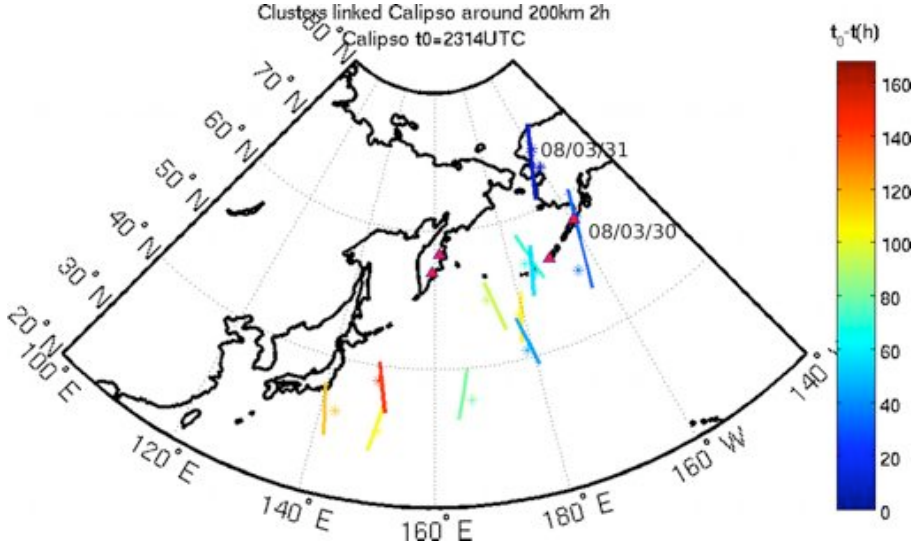

Fig. 8. Calipso track sections (line) and FLEXPART air mass positions (*) along FLEXPART trajectories initialized in the boxes $B_{F9}1$ and $B_{F9}2$ of Fig. 7a, c. The color scale indicates the elapsed time in hours between the CALIPSO observation and the aircraft observation.

ACPD
13, 4331–4389, 2013

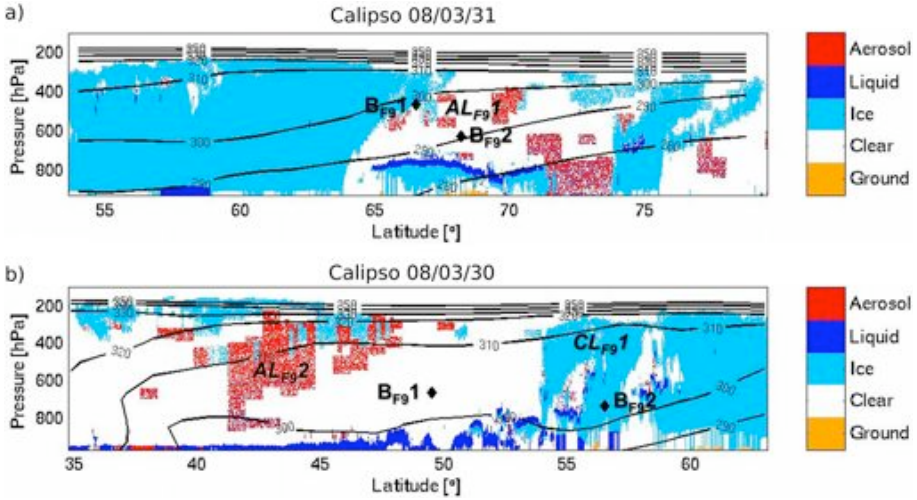

Fig. 9. Dardar Mask track section observed on 31 March **(a)** at 13:50 :00 UTC and on 30 March **(b)** at 13:05:00 2008 from of the synergistic Cloudsat radar and CALIPSO lidar, with FLEXPART air masses ($B_{F9}1$ and $B_{F9}2$) positions (♦).

ACPD
13, 4331–4389, 2013

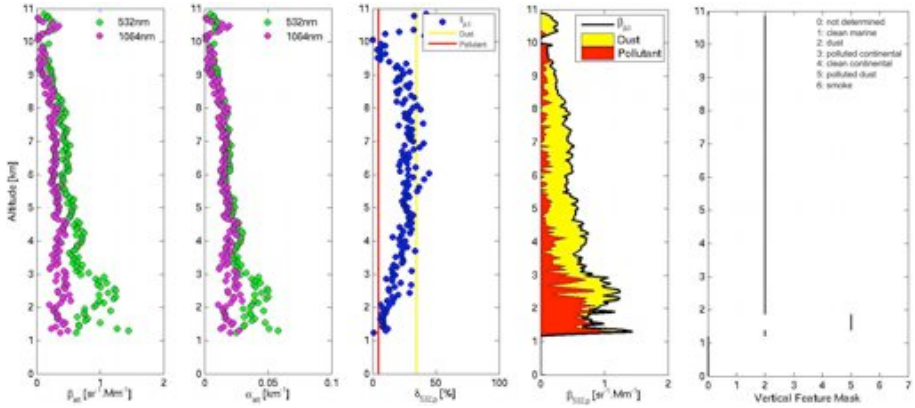

Fig. 10. (a) Total particulate backscatter coefficient at 532 nm (green) and 1064 nm (magenta); **(b)** particulate extinction coefficient at 532 nm (green) and 1064 nm (magenta); **(c)** total particulate depolarization ratio at 532 nm (green) and the input values of dust (yellow) and anthropogenic (red) particles, **(d)** separation of dust (yellow) and anthropogenic (red) particulate backscatter coefficients at 532 nm and **(e)** Vertical Feature Mask as given by CALIPSO from aerosols layer ($AL_{F9}2$) indicated in Fig. 9.

ACPD
13, 4331–4389, 2013

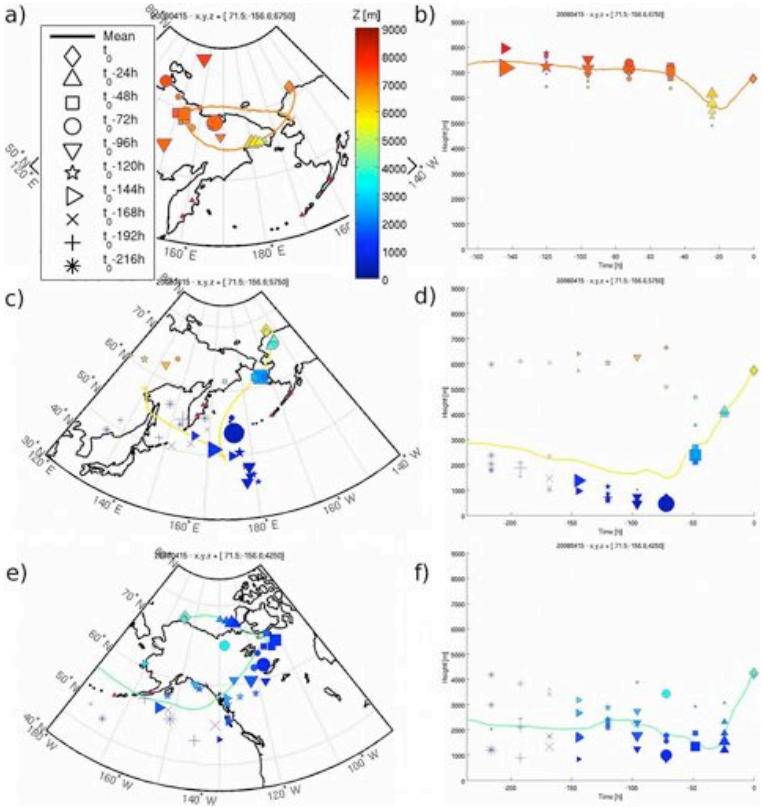

Fig. 11. 10-days backward-trajectories from FLEXPART simulations initialized on 15 April 2008 at 01:16:00 UTC for boxes located at 71.5° N; 156.6° W at **(a, b)** 6.75 km in heigth ($B_{F21}1$); **(c, d)** 5.75 km heigth ($B_{F21}2$) and **(e, f)** 4.25 km heigth ($B_{F21}3$). Clusters of particles are represented every 24 h from the beginning of the simulation. The colorbar represents the altitude of cluster in meters. Particles are released during one hour.

ACPD
13, 4331–4389, 2013

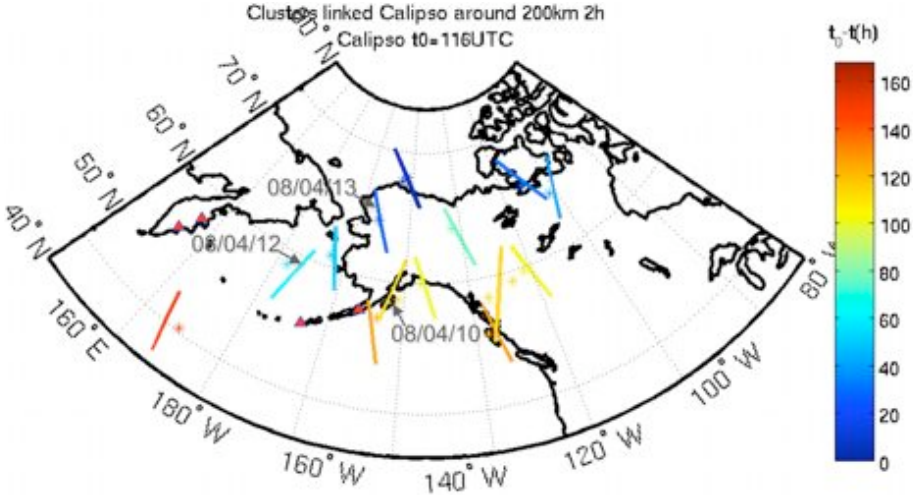

Fig. 12. Calipso track sections (line) and FLEXPART air mass positions (*) along FLEXPART trajectories initialized in the box BF212 of Fig. 11c (left of the dashed line) and initialized in the box BF213 of Fig. 11e (rigth of the dashed line). The color scale indicates the elapsed time in hours between the CALIPSO observation and the aircraft observation.

ACPD
13, 4331–4389, 2013

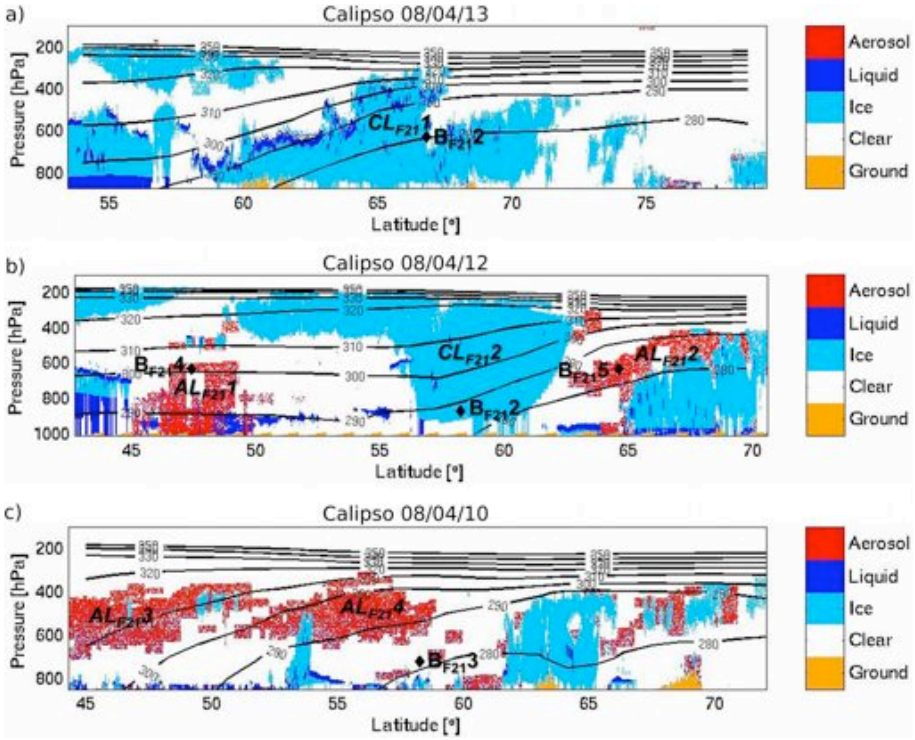

Fig. 13. Dardar Mask track section observed on 13 April **(a)** at 23:01:00 UTC, on 12 April **(b)** at 14:18:00 UTC that intercept the FLEXPART air masses ($B_{F21}2$) in positions (♦), and on 10 April **(c)** at 13:00:00 UTC that intercept the FLEXPART air masses ($B_{F21}3$) in positions (♦).

ACPD
13, 4331–4389, 2013

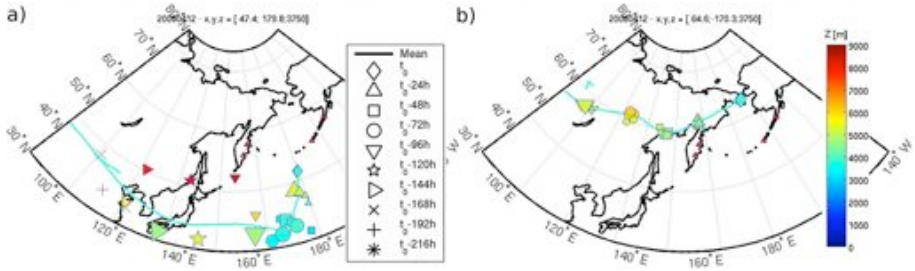

Fig. 14. 10-days backward-trajectories from FLEXPART simulations initialized on 12 April 2008 at 14:18:00 UTC for boxes BF214 located at 47.4° N; 179.8° W at 3.75 km in heigth **(a)** and BF215 located at 64.6° N; −170.3° W at 3.75 km in heigth **(b)**. Clusters of particles are represented every 24 h from the beginning of the simulation. The colorbar represents the altitude of cluster in meters. Particles are released during one hour.

ACPD
13, 4331–4389, 2013

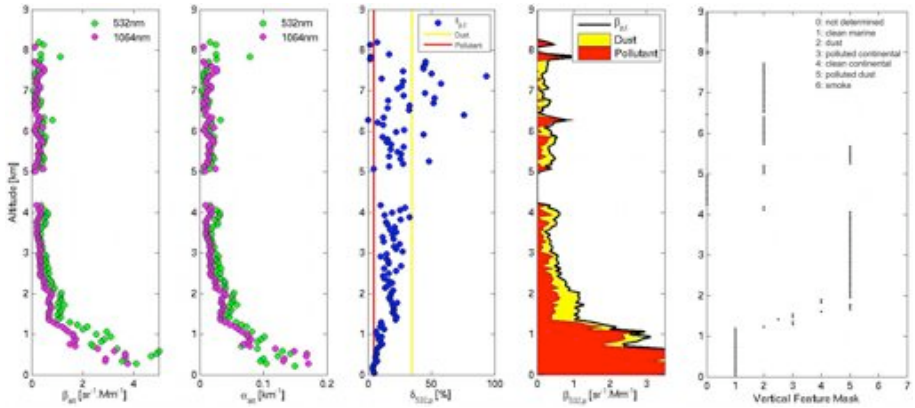

Fig. 15. (a) Total backscatter coefficient at 532 nm (green) and 1064 nm (magenta); **(b)** particulate extinction coefficient at 532 nm (green) and 1064 nm (magenta); **(c)** total particulate depolarization ratio at 532 nm (green) and the input values of dust (yellow) and anthropogenic (red) particles, **(d)** separation of dust (yellow) and anthropogenic (red) backscatter coefficients at 532 nm and **(e)** Vertical Feature Mask as given by CALIPSO from aerosols layer ($AL_{F21}1$) indicated in Fig. 13.

ACPD
13, 4331–4389, 2013

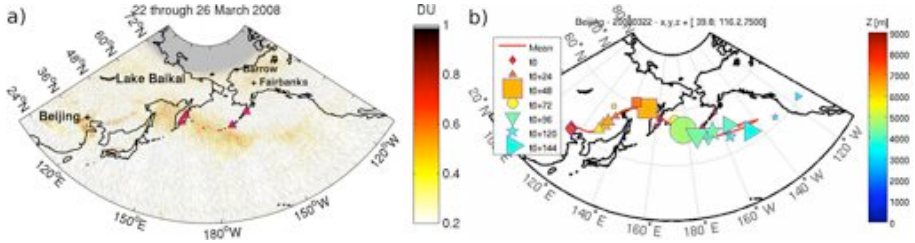

Fig. 16. Average total column density SO_2 from 22 to 26 March 2008 from Level 2G daily gridded ($0.125 \times 0.125^{\circ}$) OMI SO_2 products in the Mid-Troposphere **(a)** and 7-days forward trajectories from FLEXPART simulations initialized the 22 March 2008 at 12:00:00 UTC from Beijing in Mid-Tropophere. Clusters of particles are represented every 24 h from the beginning of the simulation. The color bar represents the altitude of cluster in meters. Particles are released during one hour.

ACPD
13, 4331–4389, 2013